1989

A Study of Oxygen Precipitation in Heavily Doped Silicon

Robert Kurt Graupner
Portland State University

A STUDY OF OXYGEN PRECIPITATION IN HEAVILY DOPED SILICON

by

ROBERT KURT GRAUPNER

A dissertation submitted in partial fulfillment of the
requirements for the degree of

DOCTOR OF PHILOSOPHY
in
ENVIRONMENTAL SCIENCES/RESOURCES PROGRAM:
PHYSICS

Portland State University

TO THE OFFICE OF GRADUATE STUDIES:

The members of the Committee approve the dissertion of Robert K. Graupner presented December 5, 1988.

[redacted]

Jack S. Semura, Advisor

[redacted]

Erik Bodegom

[redacted]

Pavel K. Smejtek

[redacted]

Stanley S. Hillman

[redacted]

David K. Roe

[redacted]

James A. Moreland

[redacted]

Faris Badi'i

APPROVED:

[redacted]

Pavel K. Smejtek, Director of ESR Program

[redacted]

Bernard Ross, Vice Provost for Graduate Studies

ACKNOWLEDGEMENTS

It is impossible to mention the many people who have contributed to or influenced the development of this dissertation. However, I particularly wish to thank Professor Jack Semura for his advice and confidence, Dr. Jim Moreland for providing his silicon expertise to my committee and to me, Wacker Siltronic Corporation for their commitment to the professional development of their employees, and to my parents Robert and Evelyn Graupner for their support and encouragement over the decades.

AN ABSTRACT OF THE DISSERTATION OF Robert K. Graupner for the Doctor of Philosophy in Environmental Sciences and Resources/Physics presented December 5, 1988.

Title: A Study of Oxygen Precipitation in Heavily Doped Silicon

APPROVED BY THE MEMBERS OF THE DISSERTATION COMMITTEE:

[redacted]

Jack S. Semura, Advisor

[redacted]

Erik Bodegom

[redacted]

Pavel K. Smejtek

[redacted]

Stanley S. Hillman

[redacted]

David K. Roe

[redacted]

James A. Moreland

[redacted]

Faris Badi'i

Gettering of impurities with oxygen precipitates is widely used during the fabrication of semiconductors to improve the performance and yield of the devices. Since the effectiveness of the gettering process is largely dependent on the initial interstitial oxygen concentration, accurate measurements of this parameter are of considerable importance. Measurements of interstitial oxygen following thermal cycles are required for development of semiconductor fabrication processes and for research into the mechanisms of oxygen precipitate nucleation and growth. Efforts by industrial associations have led to the development of standard procedures for the measurement of interstitial oxygen in wafers. However practical oxygen measurements often do not satisfy the requirements of such standard procedures. An additional difficulty arises when the silicon wafer has a low resistivity (high dopant concentration). In such cases the infrared light used for the measurement is severely attenuated by the electrons or holes introduced by the dopant. Since such wafers are the substrates used for the production of widely used epitaxial wafers, this measurement problem is economically important. Alternative methods such as Secondary Ion Mass Spectroscopy or Gas Fusion Analysis have been developed to measure oxygen in these cases. However, neither of these methods is capable of distinguishing interstitial oxygen from precipitated oxygen as required for precipitation studies.

In addition to the commercial interest in heavily doped silicon substrates, they are also of interest for research into the role of point defects in nucleation and precipitation processes. Despite considerable research effort, there is still disagreement concerning the type of point defect and its role in semiconductor

processes. Studies of changes in the interstitial oxygen concentration of heavily doped and lightly doped silicon wafers could help clarify the role of point defects in oxygen nucleation and precipitation processes. This could lead to more effective control and use of oxygen precipitation for gettering.

One of the principal purposes of this dissertation is the extension of the infrared interstitial oxygen measurement technique to situations outside the measurement capacities of the standard technique. These situations include silicon slices exhibiting interfering precipitate absorption bands and heavily doped n-type silicon wafers. A new method is presented for correcting for the effect of multiple reflections in silicon wafers with optically rough surfaces. The technique for the measurement of interstitial oxygen in heavily doped n-type wafers is then used to perform a comparative study of oxygen precipitation in heavily antimony doped (.035 ohm-cm) silicon and lightly doped p-type silicon. A model is presented to quantitatively explain the observed suppression of defect formation in heavily doped n-type wafers.

TABLE OF CONTENTS

LIST OF TABLES

LIST OF FIGURES

CHAPTER I

INTRODUCTION

Widespread utilization of semiconductor based solar cells will depend on the availability of inexpensive and high-efficiency devices. Low cost purification of metallurgical grade silicon and specialized crystal growth techniques are being developed to meet this goal (1). A problem common to several of these techniques is the presence of metallic impurities in the final product. A promising approach to this resource related problem involves the use of oxygen precipitates. Metallic impurities form levels deep in the band gap of the semiconductor which lower efficiency of the solar cell by reducing the minority carrier lifetime (2). The introduction of process steps during which the impurities are precipitated or gettered improves the lifetime and the cell efficiency (3). Such gettering can occur when interstitially dissolved oxygen undergoes a phase change resulting in the nucleation and growth of SiO_2 precipitates and the formation of dislocation networks (4). While oxygen precipitates in the bulk have this beneficial effect, those in the vicinity of the solar p-n junction degrade performance. To avoid this detrimental effect, a precipitate and defect-free region at the device surface is required. Such a region, which is referred to as a denuded zone, can be formed by control of the thermal cycles, ambients, and the initial oxygen content of the

silicon (5).

Gettering of impurities with oxygen precipitates is widely used during the fabrication of semiconductors to improve the performance and yield of the devices (5). Since the effectiveness of the gettering process is largely dependent on the initial interstitial oxygen concentration, accurate measurements of this parameter are of considerable importance. Measurements of interstitial oxygen following thermal cycles are required for development of semiconductor fabrication processes and for research into the mechanisms of oxygen precipitate nucleation and growth. Efforts by industrial associations such as the American Society for Testing and Materials (ASTM) have led to the development of standard procedures for the measurement of interstitial oxygen in wafers which are mirror polished on both surfaces (6). Unfortunately, in practice the surfaces of silicon wafers often do not satisfy the requirements of such standard procedures. An additional difficulty arises when the silicon wafer has a low resistivity (high dopant concentration). In such cases the infrared light used for the measurement is severely attenuated by the electrons or holes introduced by the dopant. Since such wafers are the substrates used for the production of widely used epitaxial wafers, this measurement problem is economically important. Alternative methods such as Secondary Ion Mass Spectroscopy (7) or Gas Fusion Analysis (8) have been developed to measure oxygen in these cases. However, neither of these methods is capable of distinguishing interstitial oxygen from precipitated oxygen as required for precipitation studies.

In addition to the commercial interest in heavily doped silicon substrates, they are also of interest for research into the role of point defects in nucleation and precipitation processes. Despite considerable research effort, there is still disagreement concerning the type of point defect and its role in semiconductor processes. Vacancies can exist in charged as well as neutral states (9), so processes involving vacancies may be affected by the fraction of vacancies which exist in different charge states, and that is in turn determined by the dopant concentration. Studies of changes in the interstitial oxygen concentration of heavily doped and lightly doped silicon wafers could help clarify the role of point defects in oxygen nucleation and precipitation processes. This could lead to more effective control and use of oxygen precipitation for gettering.

One of the principal purposes of this thesis is the extension of the infrared interstitial oxygen measurement technique to situations outside the measurement capacities of the standard technique. These situations include silicon slices with non-polished surfaces, silicon slices exhibiting interfering precipitate absorption bands and heavily doped n-type silicon wafers. This is accomplished in Chapters II and III. A technique for the measurement of interstitial oxygen in heavily doped silicon enables determination of the effect of dopant concentrations on oxygen precipitation and development of a model explaining the previously observed suppression of bulk defect creation in heavily doped n-type wafers. This is accomplished in Chapter IV. The results of this thesis research are summarized in Chapter V.

CHAPTER II

INFRARED MEASUREMENT OF OXYGEN IN LIGHTLY DOPED SILICON

The principal technique for measuring interstitial oxygen in semiconductor-grade silicon is infrared absorption using Fourier Transform Infrared (FTIR) spectrometry (10,11). Measurements of interstitial oxygen before and after thermal cycles indicate the degree to which oxygen has diffused out of the silicon or changed from the interstitial phase to an SiO_2 phase during thermal processing (12). Characterization and optimization of the behavior of oxygen in silicon during the manufacture of semiconductor devices requires accurate measurements of oxygen in both virgin and processed silicon wafers.

Section 2.1 discusses the measurement used for silicon slices with optically smooth surfaces on both sides. This is the technique used to measure the oxygen content of samples from silicon crystals prior to processing the ingots into polished slices. Accurate measurements in these cases require consideration of the fraction of light which, due to surface reflection, passes through the slice multiple times. Unfortunately, the silicon slices which are used to manufacture semiconductor devices typically have only one side optically smooth with the other side being optically rough. Much of the material used for this research falls into that class. For these cases the techniques developed in Section 2.1 are not directly applicable.

Section 2.2 presents a general method developed by the author to account for multiple reflections in slices with arbitrary surface finishes.

Measurement of the interstitial oxygen remaining after a large fraction has precipitated into the SiO_2 phase also presents measurement difficulties. The infrared absorption bands due to the SiO_2 precipitates overlap and obscure the absorption bands due to interstitial oxygen. These overlapping absorption bands can be separated by cooling the silicon sample to temperatures near 0°K prior to measurement (13). This is not practical for routine measurements. Section 2.3 presents a method which can remove much of the overlapping SiO_2 absorption bands allowing for accurate interstitial oxygen measurements at room temperature.

The measurement of oxygen in heavily doped material has special difficulties which are discussed in Chapter III.

The infrared measurements provide a value for the absorption coefficient α_{ox} due to interstitial oxygen. The oxygen concentration in atoms/cm^3 or as a fraction of the total atoms present in parts per million (ppma) is obtained by multiplying α_{ox} by a conversion factor. The conversion factor has been revised several times and the four different factors in wide use for measurements at 300°K are given below (6):

Old ASTM	ppma = $9.63\alpha_{OX}$
(ASTM F121-79)	atoms/cm^3 = $4.81 \times 10^{17}\alpha_{OX}$
New ASTM	ppma = $4.9\alpha_{OX}$
(ASTM F121-83)	atoms/cm^3 = $2.45 \times 10^{17}\alpha_{OX}$
JEIDA	ppma = $6.1\alpha_{OX}$
	atoms/cm^3 = $3.03 \times 10^{17}\alpha_{OX}$
IOC-88	ppma = $6.28\alpha_{OX}$
	atoms/cm^3 = $3.14 \times 10^{17}\alpha_{OX}$

All oxygen concentrations reported in this work use the Old ASTM conversion factor unless otherwise stated.

2.1 MEASUREMENT OF DOUBLE-SIDED POLISHED SILICON SAMPLES

The simplest formula relating transmittance T or absorbance A ($A = -\log_{10}T$)to the absorption coefficient α for a sample of thickness d is (14):

$$T = (1-R)^2 \exp(-\alpha d) \qquad 2.1a$$

$$A = -\log_{10}(1-R)^2 + (\alpha d/2.303) \qquad 2.1b$$

where R is the reflectance which is 0.3 for lightly doped silicon. The absorption coefficient obtained from either of equations 2.1 for the absorption band in silicon at 1105 cm^{-1} is the sum of three contributions (15,16):

$\alpha = \alpha(ox) + \alpha(l) + \alpha(el)$ where:

$\alpha(ox)$ = The absorption coefficient due to the interstitial oxygen.

$\alpha(l)$ = The value of the intrinsic lattice absorption band at 1105 cm^{-1}.

$\alpha(el)$ = The value of the free carrier absorption at 1105 cm^{-1} due to the electrons and holes in the silicon.

The term $\alpha(el)$ is a function of the resistivity of the material and is usually ignored for lightly doped ($N < 1 \times 10^{16} cm^{-3}$) material (16). The combined absorption band and the intrinsic band alone are shown in Figure 1. The intrinsic absorption spectrum is obtained from a silicon sample containing negligible oxygen prepared by the float zone method.

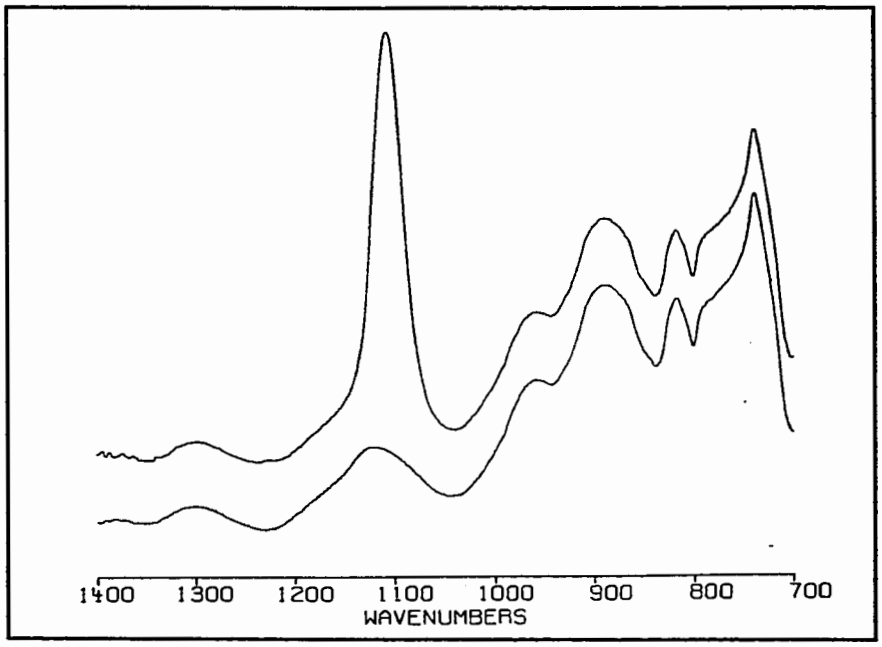

Figure 1. Intrinsic silicon absorption spectrum (bottom) and spectrum of silicon containing oxygen (top).

The absorption band due to the interstitial oxygen can be obtained from the combined absorption band by subtracting a float zone silicon absorption spectrum from the sample absorption spectrum where the thickness of the float zone reference is equal to the sample thickness (17). The elimination of the intrinsic absorption bands which are common to both spectra creates a flat baseline from which the oxygen absorption band height can be measured. Figure 2 shows the sample spectrum of Figure 1 after subtraction of the float zone silicon spectrum. An expression for $\alpha(ox)$ in this case can be obtained by writing 2.1b for the sample with $\alpha = \alpha(ox) + \alpha(l)$ and for the float zone reference with $\alpha = \alpha(l)$ and then subtracting these expressions. The result is:

$$\alpha(ox) = (2.303/d)H \qquad 2.2$$

where H is the peak height from the baseline in absorbance units.

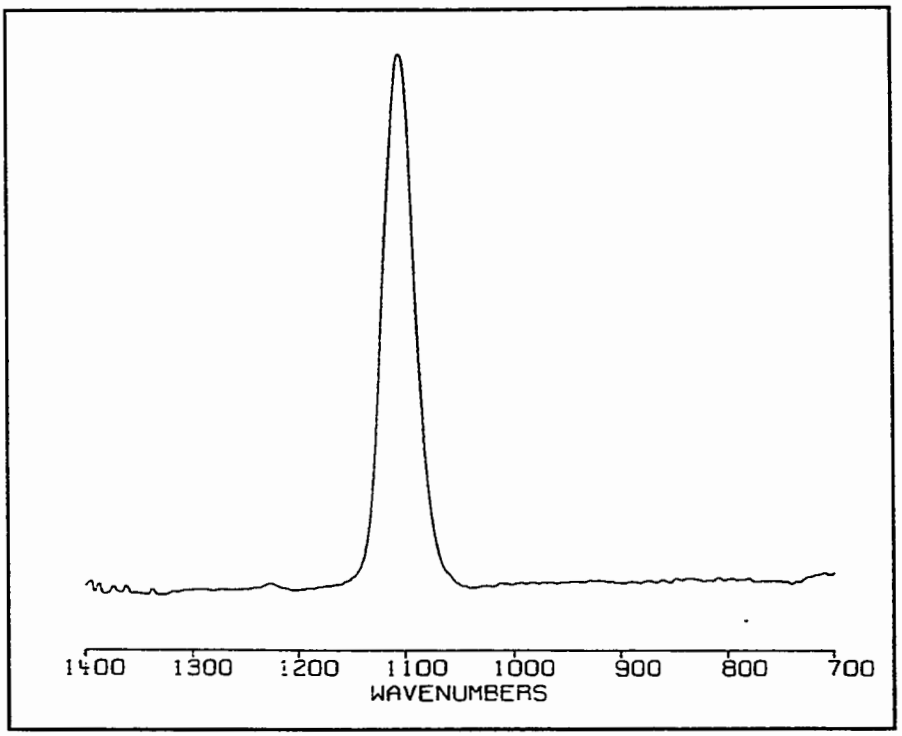

Figure 2. Spectrum of silicon with interstitial oxygen after subtraction of a float zone silicon spectrum.

Equation 2.2 is often applied to the measurement of silicon slices with one optically flat surface and one optically rough surface. If the sample surfaces are both optically smooth, a fraction of the light reflected from the second surface will be reflected back by the first surface. Some of this re-reflected light will reach the detector and increase the transmittance above the value predicted by equation 2.1a. This multiple reflection process is illustrated in Figure 3.

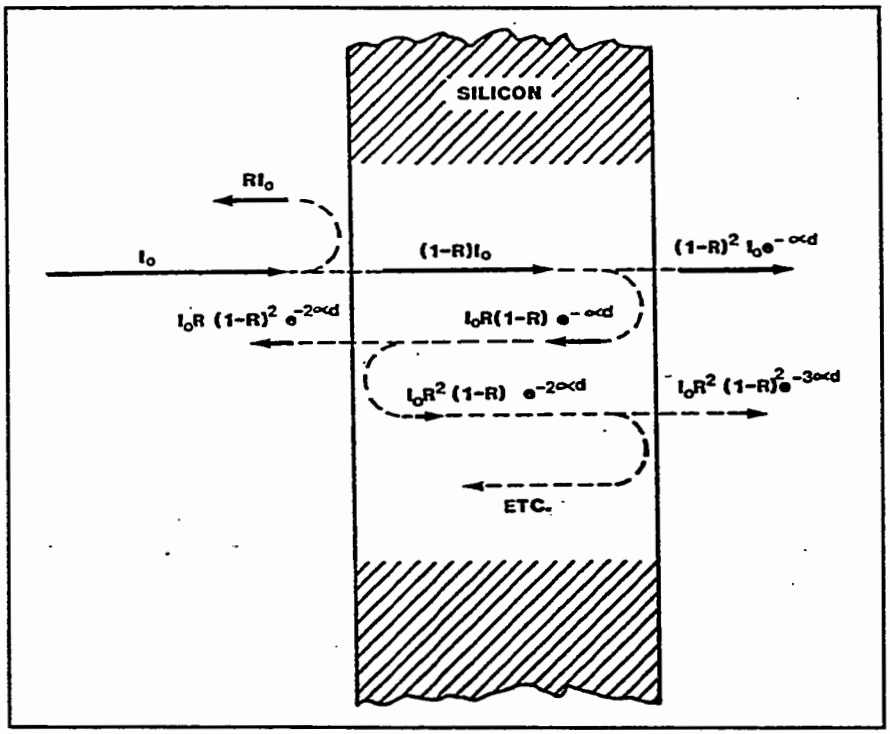

Figure 3. Effect of multiple reflections on transmittance.

The infinite series of terms shown in Figure 3 can be summed to yield (17):

$$T = (1-R)^2 \exp(-\alpha d)/(1-R^2 \exp(-2\alpha d)) \qquad 2.3$$

Using the quadratic formula to solve 2.3 for $\exp(-\alpha d)$ and then taking the ln of both sides of the equation yields:

$$\alpha = d^{-1}(-\ln(T/(1-R)^2) + \ln((1+(1+4R^2T^2(1-R)^{-4})^{1/2})/2)) \qquad 2.4$$

Equation 2.3 can be written:

$$\alpha = d^{-1}(-\ln(T/(1-R)^2) + C(\alpha d)) \qquad 2.5$$

Equation 2.5 is of the form of equation 2.1a with the addition of the multiple reflections correction term $C(\alpha d)$ given by

$$C(\alpha d) = -\ln(1-R^2 \exp(-2\alpha d))$$

Comparing equation 2.4 and 2.5 gives us the identity

$$C(\alpha d) = \ln(1/(1-R^2 \exp(-2\alpha d))) = \ln((1+(1+4R^2T^2(1-R)^{-4})^{1/2})/2) \qquad 2.6$$

Equation 2.6 enables us to evaluate the multiple reflection correction term from the transmittance plot since the right hand side requires only T. We can then use this value in equation 2.5 to obtain the correct value for α.

If we make peak height measurements from a baseline drawn on an absorption spectrum we must consider the effects of two correction terms. One term corrects the absorbance at the peak while the second term corrects the absorbance at the baseline. The net effect can be considered to be a stretching of the absorption band between the baseline and the peak. This is shown graphically in Figure 4.

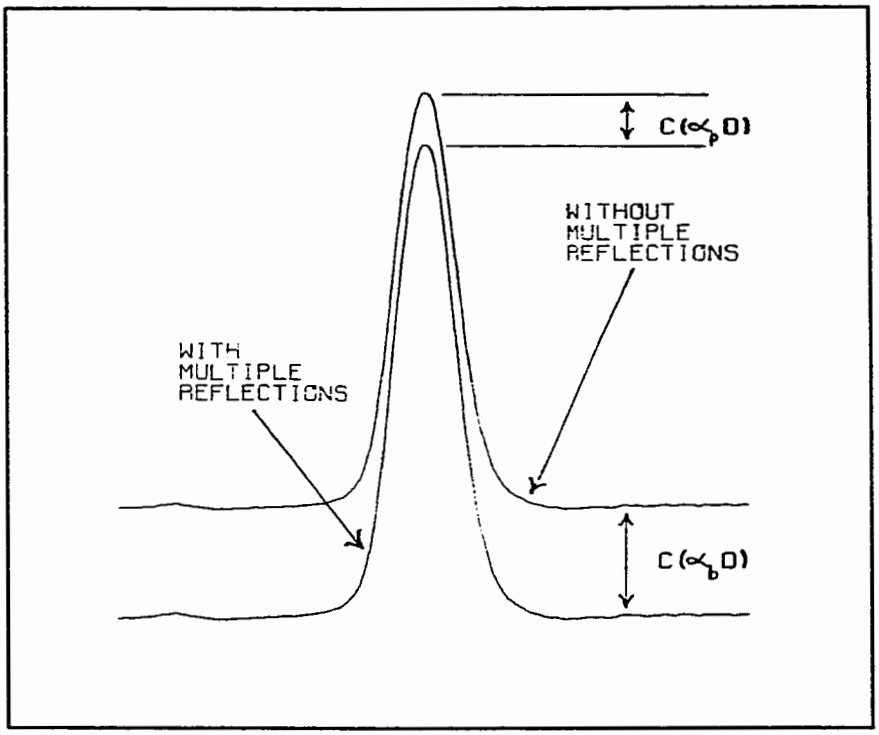

Figure 4. Change in measured peak height due to effect of multiple reflections.

To derive the equation describing this situation we first write equation 2.3 in absorbance units A:

$$A = (\alpha d/2.303) - C(\alpha d)/2.303 - \ln((1-R)^2)/2.303 \qquad 2.7$$

Using equation 2.7 to obtain the measured absorbance at the peak A_p and the measured absorbance at the baseline A_b and subtracting yields:

$$H = A_p - A_b = (\alpha_p - \alpha_b)d/2.303 + C(\alpha_b d)/2.303 - C(\alpha_p d)/2.303 \qquad 2.8$$

Here H is the peak height in absorbance units obtained from measurements on the sample spectrum. The first term on the right side of equation 2.8 is the peak

height in absorbance units which would be measured in the absence of multiple reflections. The next term increases H to account for the lowered baseline absorbance and the last term reduces H to account for the lowered peak absorbance. The term C(αd) is plotted in Figure 5. Over the range of αd from 0.0 to 0.3[1] this function can be well approximated by the linear equation:

$$C(\alpha d) = B - g\alpha d \qquad 2.9$$

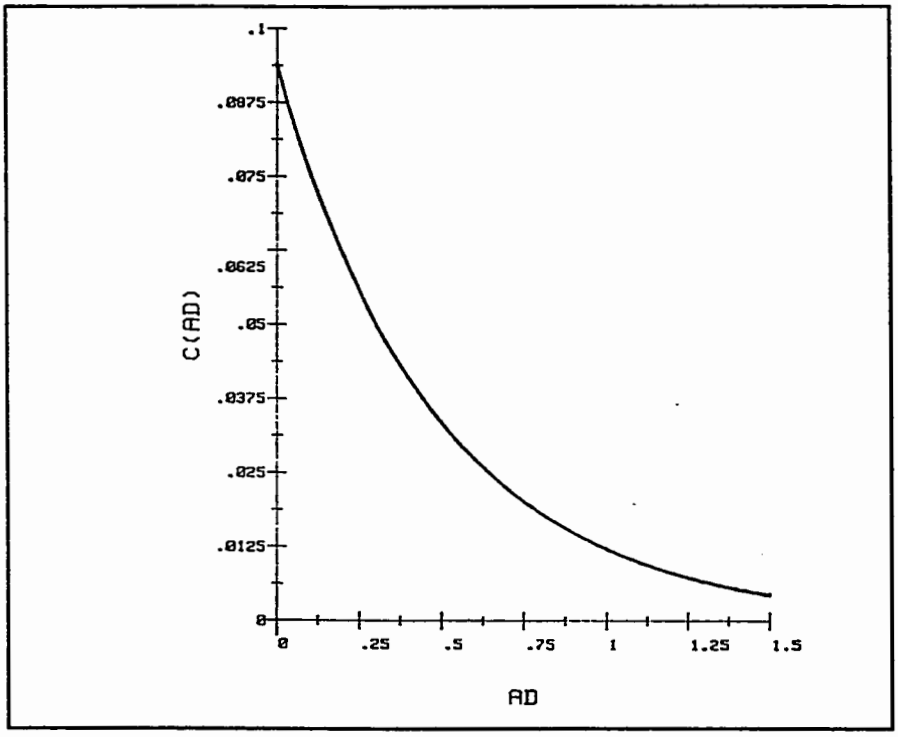

Figure 5. Multiple reflection correction term C(αd) as a function of αd.

[1]The maximum value of αd = 0.3 corresponds to a 650 micron thick slice with an oxygen content of 43 ppma.

Substituting equation 2.9 into 2.8 yields:

$$\alpha_p - \alpha_b = 2.303H/d(1+g) = 2.303H/d_{eff} \qquad 2.10$$

Equation 2.10 is the same equation as would be obtained by neglecting the effect of multiple reflections and applying equation 2.2 to a sample of effective thickness $d_{eff} = d(1+g)$. Thus for thin slices where approximation 2.9 is valid the effect of multiple reflections can be accounted for by using an effective thickness in the simple equation 2.2.

The coefficient g in equation 2.9 is the slope of the tangent to the C(αd) curve shown in figure 5. We can obtain g by evaluating the derivative of C(αd) with respect to αd:

$$\frac{dC(\alpha d)}{d(\alpha d)} = g = 2R^2\exp(-2\alpha d)/(1-R^2\exp(-2\alpha d)) \qquad 2.11a$$

$$= 2((1-R^2\exp(-2\alpha d))^{-1}-1) \qquad 2.11b$$

Using equation 2.6 this becomes

$$g = -1 + (1 + 4R^2T^2(1-R)^{-4})^{1/2} \qquad 2.11c$$

To minimize the error incurred in the linear approximation 2.9, g should be evaluated at a value which is the average of the known value of αd at the baseline and the expected value of αd at the peak.

Equation 2.8 can be generalized for the case where a reference spectrum is subtracted from a sample spectrum and both reference and sample have optically smooth surfaces. As mentioned earlier, this is the procedure used to separate the silicon lattice absorption band from the interstitial oxygen absorption band. In the general case, the reference spectrum is multiplied by d(s)/d(r) where d(s) is the thickness of the sample and d(r) is the thickness of the reference. This accounts for thickness differences between the sample and reference. In generalizing equation 2.8 we must be careful to account for the effect of multiple reflections by applying equation 2.5 to both sample and reference spectra:

$$2.303H = 2.303(H(s) - (d(s)/d(r))H(r))$$

$$= (\alpha(p,s) - \alpha(b,s))d(s) + C(\alpha(b,s)d(s)) - C(\alpha(p,s)d(s)) - (\alpha(p,r) - \alpha(b,r))d(s) - (d(s)/d(r))(C(\alpha(b,r)d(r)) - C(\alpha(p,r)d(r)))$$

The labels p,b,r,s refer to peak, baseline, reference and sample respectively. This equation can be simplified if the sample thickness is the same as the reference thickness $d(r) = d(s) = d$ and the free carrier absorption is negligible. In this case. $\alpha(b,r) = \alpha(b,s)$ and we have:

$$2.303H = (\alpha(p,s) - \alpha(p,r))d - C(\alpha(p,s)d) + C(\alpha(p,r)d)$$

With $\alpha(p,s) = \alpha(ox) + \alpha(l)$ and $\alpha(p,r) = \alpha(l)$ this becomes:

$$2.303H = \alpha(ox)d + \ln(1-R^2\exp(-2(\alpha(ox) + \alpha(l)))) - \ln(1-R^2\exp(-2\alpha(l)))$$

This equation can be solved for $\alpha(ox)$ using the quadratic equation (16).

2.2 MEASUREMENT OF SILICON SLICES WITH OPTICALLY ROUGH SURFACES

The previous section described two basic equations which can be used to obtain $\alpha_{OX}$from absorption spectra. Equation 2.1a ignores the effect of multiple reflections on the absorption spectrum. It is applicable to samples with very rough surfaces that effectively scatter any multiply reflected light out of the beam that is focussed on the detector. Equation 2.3 is applicable to slices with optically smooth surfaces. In such slices all of the multiply reflected light reaches the detector. Unfortunately, many of the slices used in semiconductor manufacturing or research fall in between these two extreme cases.

The usefulness of the "effective thickness method" is its applicability to the measurement of slices which cannot be accurately described by either equation 2.1a or equation 2.3. Such slices show smaller transmittance in regions where $\alpha d = 0$ than the 53.8% predicted by equation 2.3 but larger transmittance than the 49% predicted by equation 2.1a. For these slices the multiply reflected light has been attenuated by scattering, but not eliminated. Use of equation 2.1a will yield oxygen concentrations higher than the actual values while equation 2.3 will yield concentrations lower than the actual values.

To apply the "effective thickness method" we do not need to know the functional form of the correction term $C(\alpha d)$, but only need to assume that $C(\alpha d)$ can be reasonably approximated by a linear equation of the form of equation 2.9.

The value of d_{eff} can be experimentally obtained by measuring the degree of "stretching" of the intrinsic absorption bands located near the 1105 cm^{-1} interstitial oxygen absorption band. This is done by performing a spectral subtraction of a float zone reference absorption spectrum multiplied by a scale factor from the sample absorbance spectrum. The scale factor is adjusted until the selected intrinsic absorption band is eliminated, leaving only the slowly varying baseline due to the backside scattering. On modern computerized FTIR spectrometers, this subtraction can be performed interactively while viewing the result on a CRT. When the intrinsic bands are eliminated the following condition is satisfied:

$$d_{eff}(\text{sample}) = (\text{scale factor})\ d_{eff}(\text{reference}) \qquad 2.12$$

The term d_{eff}(sample) is then used with equation 2.2 to calculate α_{ox}. The condition of equation 2.12 also creates the flat baseline since it eliminates the intrinsic bands which overlap the interstitial oxygen band. By using a double-side polished float zone silicon reference slice the effective thickness of the reference d_{eff}(reference) can be evaluated using

$$d_{eff}(\text{reference}) = d_0(1+g)$$

where d_0 is the physical thickness of the reference slice and the value of g is obtained from equation 2.11 using a value of αd which is the average of the peak and baseline values $\alpha_p d$ and $\alpha_b d$ for the intrinsic absorption band which is chosen to be subtracted out.

As an alternative, we could use a reference spectrum which has been corrected for the effects of multiple reflections. From equation 2.3, we could calculate the transmittance value T_{cor} which would be obtained in the absence of multiple reflections:

$$T_{cor} = T(1-R^2\exp(-2\alpha d) \qquad 2.13$$

Using the value R = 0.3 in equation 2.6, equation 2.13 becomes:

$$T_{cor} = T/(0.5+0.5(1+1.5T^2)^{1/2})$$

Appendix A has the listing of a program titled MRC which performs this calculation on spectra stored in the memory of the NICOLET 6000 spectrometer. When the reference absorption spectrum is obtained in this manner then

$$d_{eff}(\text{reference}) = d_0(\text{reference})$$

and the effective thickness of the absorption spectrum obtained from 2.13 is equal to the physical thickness.

Using the above procedure, the oxygen concentration for a slice with any back surface finish or any amount of internal scattering can be obtained using equations 2.10 and 2.12. Since the effect of the multiple reflections is experimentally measured, this procedure is not dependent upon the validity of any empirical model of the scattering.

This method assumes that the band stretching at 1105 cm^{-1} is equal to the band stretching of the nearby intrinsic bands which are used to obtain g. A series of measurements were made on a wafer to establish the validity of this assumption and to determine the effectiveness of the technique. Starting with an

initially rough backside, the wafer was successively polish etched until an optically smooth backside was obtained. Following each etching step the wafer was measured and the interstitial oxygen concentration was calculated in three ways:

1. Using the formula published by Stallhofer and Huber (16). This formula is a generalization of equation 2.4 and includes the effect of the multiple reflections on the float zone reference. The formula is valid for slices with optically smooth surfaces where all of the multiply reflected light reaches the detector. The method is referred to in Table I as DSP.

2. Using equation 2.2. This formula is valid for slices where none of the multiply reflected light reaches the detector. This method is referred to in Table 1 as SSP.

3. Using the effective thickness method described above. This method is referred to in Table 1 as ETM.

The measurements were performed on a NICOLET 6000 FTIR with a mercury-cadmium-telluride detector. Each spectrum was the sum of 32 scans at 4 cm^{-1} resolution. The transmittance spectra taken of the virgin slice and following each etching step are shown in Figure 6. It can be seen from that figure that the samples covered a wide range of transmittance with the virgin slice having the lowest transmittance.

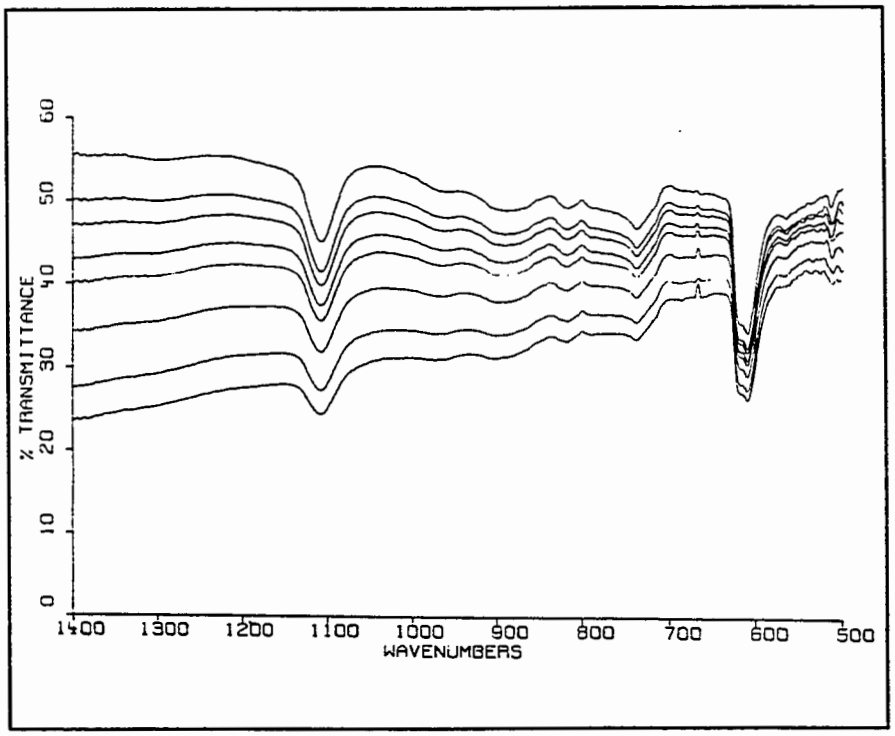

Figure 6. Transmittance spectra of a wafer after successive polish etching steps.

The intrinsic bands at 886 cm^{-1}, 819 cm^{-1}, and 739 cm^{-1} were used to determine the effective thickness of the sample. The effective thickness of the float zone reference was 496 microns. Table I gives the physical thickness of the sample at each measurement step and the oxygen concentration calculated using the three techniques described above.

TABLE I

SAMPLE THICKNESS d_0 IN MICRONS, OXYGEN CONCENTRATION IN PPMA, CALCULATED USING THE DSP, SSP AND ETM TECHNIQUES.

d_0	DSP	SSP	ETM
451	30.71	35.49	31.02
485	29.32	33.82	30.09
491	28.74	33.15	30.17
498	28.06	32.37	29.58
503	27.66	31.91	29.45
508	27.06	31.22	29.39
513	27.16	31.33	30.09
515	26.89	31.02	29.90

Assuming that the DSP method applied to the 451 micron thick mirror-polished slice yields the correct oxygen concentration, we can compare the accuracy of the three techniques. The oxygen concentration calculated using the DSP method increasingly underestimates the oxygen concentration as the roughness of the backside increases. For the 515 micron thick slice the error incurred by using the DSP method exceeds 12%. The error of the SSP method exceeds 15% for the 451 micron thick slice. As the roughness of the backside increases the error incurred by using the SSP method decreases, reaching a value of 1% for the 515 micron thick slice.

The oxygen concentration calculated using the ETM method shows the least variation. Using the ETM method the error in oxygen concentration is 1% for the mirror polished (451 micron) slice and 2.6% for the roughest backside (512 micron) slice. The maximum error that occurred for the ETM method was 4.1%.

Some of the error in the ETM method may be due to the somewhat subjective visual determination of when the intrinsic bands are eliminated leaving only the slowly varying background. Use of an objective algorithm could reduce this source of error. The oxygen concentrations reported in the following research were calculated using the ETM method.

2.3 MEASUREMENT OF THERMALLY PROCESSED SLICES

The technique of infrared absorption is routinely used to determine the interstitial oxygen concentration remaining after the thermal processing of silicon slices (13). The reduction of the interstitial oxygen concentration is attributed either to the precipitation of oxygen to a solid phase within the silicon or to diffusion to the free surface of the silicon (12). Severe distortion of the interstitial oxygen absorption peak at 1105 cm^{-1} occurs when the thermal processes cause large reduction in the initial oxygen concentration. This distortion results from the presence of oxygen precipitate absorption bands which overlap the 1105 cm^{-1} peak.

Figure 7 shows the absorption spectra of a 2 mm thick silicon slice before and after thermal processing. The slice was oxidized in dry oxygen at 750°C for six hours and then oxidized in dry oxygen at 1050°C for 24 hours. The initial oxygen concentration was 43.5 ppma. The interstitial oxygen concentration of the oxidized slice as determined by applying the standard oxygen measurement technique (14) to the distorted peak at 1105 cm^{-1} is 12.0 ppma. However, this

measurement is of questionable validity since the shape of the 1105 cm^{-1} absorption band differs substantially from the shape of the absorption band in the virgin slice. The interference due to the precipitate absorption bands can be eliminated by making the oxygen measurement at cryogenic temperatures (13). The following procedure enables the overlapping precipitate bands to be eliminated for room temperature measurements.

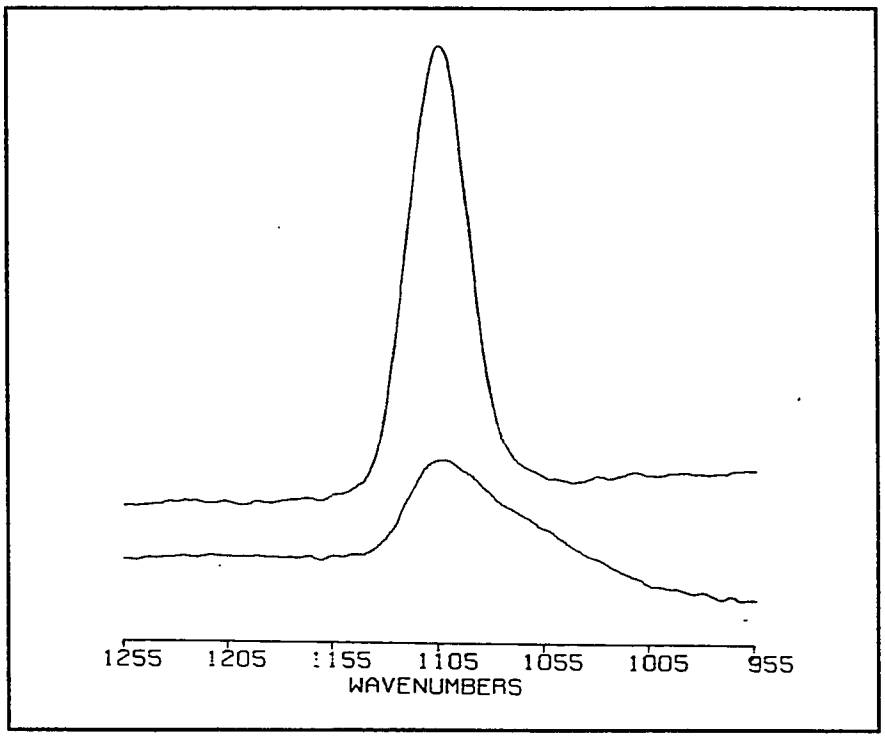

Figure 7. Spectra for a virgin silicon slice (top) and the same slice after thermal processing.

Figure 8 shows the absorption spectrum for a thermally grown silicon dioxide layer in silicon for three layer thicknesses. As may be seen from a comparison of Figures 7 and 8, the low wavenumber side of the distorted 1105 cm^{-1} absorption band is similar in shape to the absorption band near 1080 cm^{-1} of thermally grown silicon dioxide layer (18). This is reasonable since both the internal oxygen precipitates and the thermally grown layer have the same chemical composition. Figure 8 shows the spectrum of the silicon dioxide layer for several layer thicknesses. A close comparison of the distorted 1105 cm^{-1} peak of Figure 7 with the spectra in Figure 8 showed that the 349 Å thick silicon dioxide layer provided the best match to the low wavenumber side of the distorted peak.

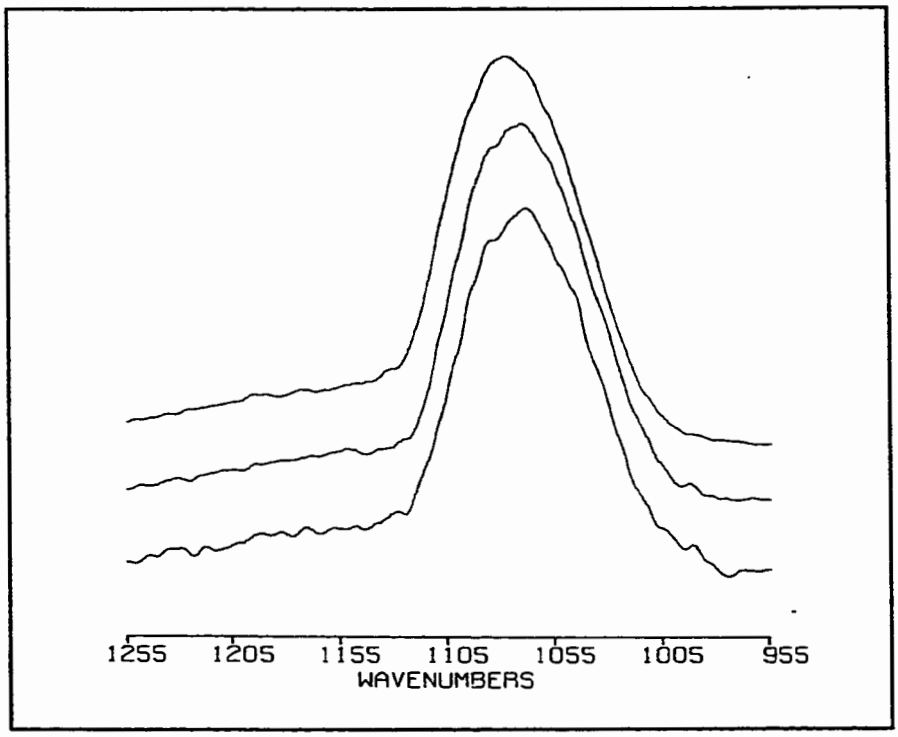

Figure 8. Spectra of silicon dioxide layer on silicon for layer thicknesses of 1600 Å (top), 508 Å (center) and 349 Å (bottom).

If we now subtract a properly scaled silicon dioxide absorption peak from the distorted absorption band in Figure 7 we will be able to eliminate the interference caused by the precipitate bands. On the NICOLET *6000* this procedure is implemented interactively by subtracting a spectrum FCR*(349Å silicon dioxide absorption spectrum) from the sample spectrum. The scale factor FCR is adjusted until the resultant spectrum has the shape of the 1105 cm^{-1} interstitial oxygen absorption peak. Figure 9 shows the result of subtracting 0.942 x (Absorption spectrum of 349 Å silicon dioxide layer) from the distorted peak of Figure 7.

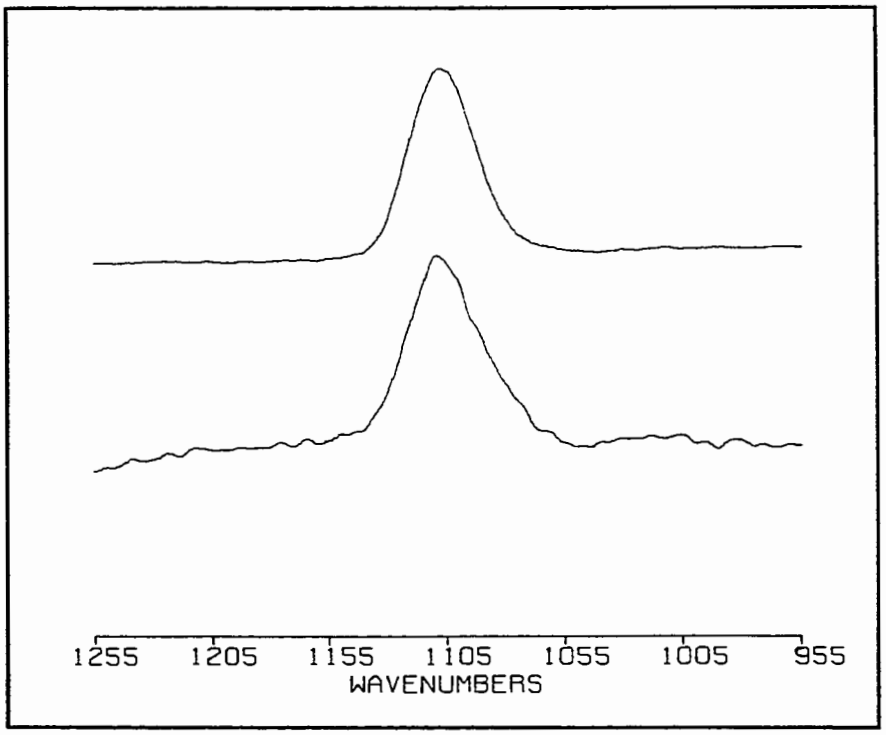

Figure 9. Spectrum of thermally processed wafer from Figure 7 after subtraction of SiO_2 spectrum (bottom). 1105 cm^{-1} interstitial oxygen (top).

This step eliminates the distortion, producing a peak with a shape very similar to the 1105 cm^{-1} absorption peak in the virgin material. A scaled 1105 cm^{-1} absorption peak from virgin silicon is included in Figure 9 for comparison purposes. The interstitial oxygen concentration calculated using the processed spectrum in Figure 9 is 10.2 ppma, a 15% reduction from the value obtained from the distorted peak. Similar results were obtained from measurements made in other heavily precipitated slices. Given the large amount of precipitation which occurred and the rather severe peak distortion, this is a surprisingly small error.

In many precipitation studies the interstitial oxygen measurements are used to compare the effects of different thermal cycles and such errors are not significant.

However, for precipitation studies which require high accuracy, either the above technique or cryogenic measurements should be used to eliminate the errors due to the overlapping precipitate bands.

CHAPTER III

INFRARED MEASUREMENT OF OXYGEN IN HEAVILY DOPED SILICON

One factor limiting the precision of quantitative infrared spectroscopic measurements is the uncertainty in peak and baseline absorbance caused by noise. The effect of noise is seldom a practical limitation for measurements of interstitial oxygen in lightly doped silicon made using FTIR spectrometers. The low noise levels of modern FTIR equipment and typically high signal levels reduce this source of error below those due to other causes such as the treatment of multiple reflections (14,19), effect of sample alignment (20), or detector nonlinearity (10).

However, the IR measurement of interstitial oxygen in heavily doped silicon presents special difficulties. Free carriers (electrons or holes) in silicon absorb infrared radiation. Figure 10 shows an open-beam background spectrum and a single-beam sample spectrum[2] for a 0.019 ohm-cm double-side polished 410-micron thick antimony-doped silicon sample illustrating the sharp reduction in signal below 2000 cm^{-1} caused by free carrier absorption.

---

[2]Each spectrum is the average of 8 scans taken at 1 cm^{-1} resolution.

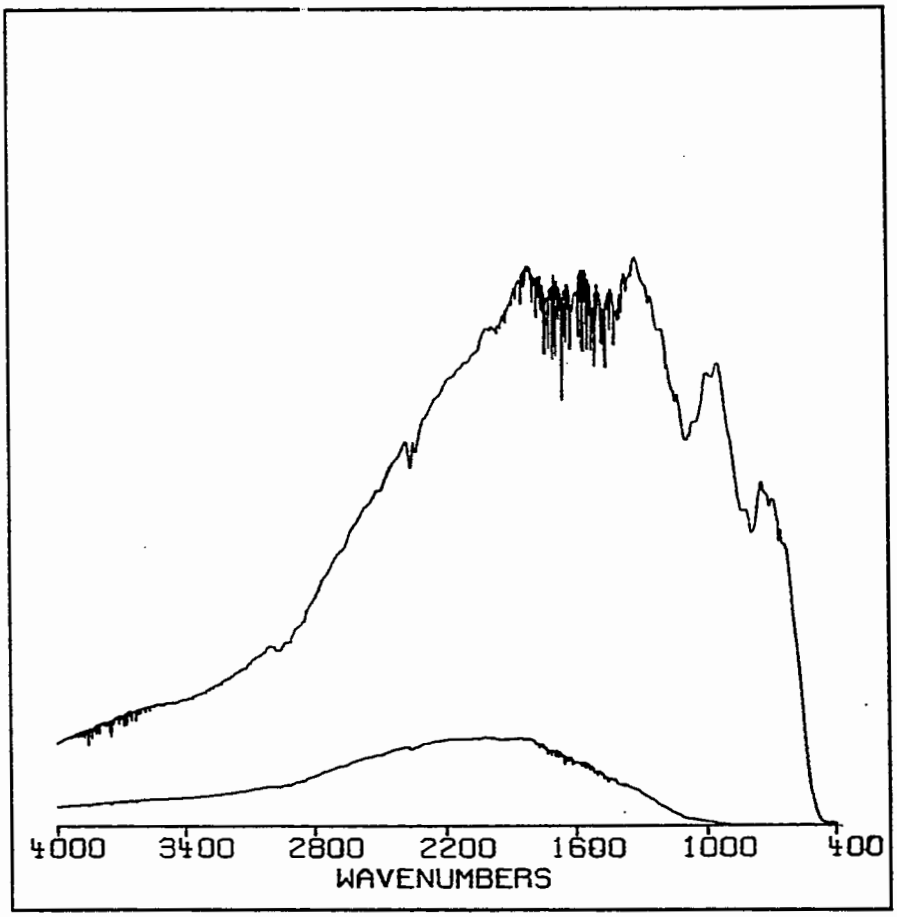

Figure 10. Single-beam spectra for open-beam background (top) and a double-side-polished 0.019 ohm-cm 410-micron-thick antimony-doped silicon sample (bottom) showing the reduction in signal intensity caused by free carrier absorption.

The signal reduction degrades the signal-to-noise ratio (S/N) of the spectrum and causes variation in the oxygen measurement since the measured peak height is the peak height due to interstitial oxygen absorption at 1105 cm^{-1} plus the amplitude of the noise spectrum at 1105 cm^{-1}. This is shown in Figure 11, where

the peak-to-peak height of the noise is a substantial fraction of the small oxygen absorption peak at 1105 cm^{-1}.

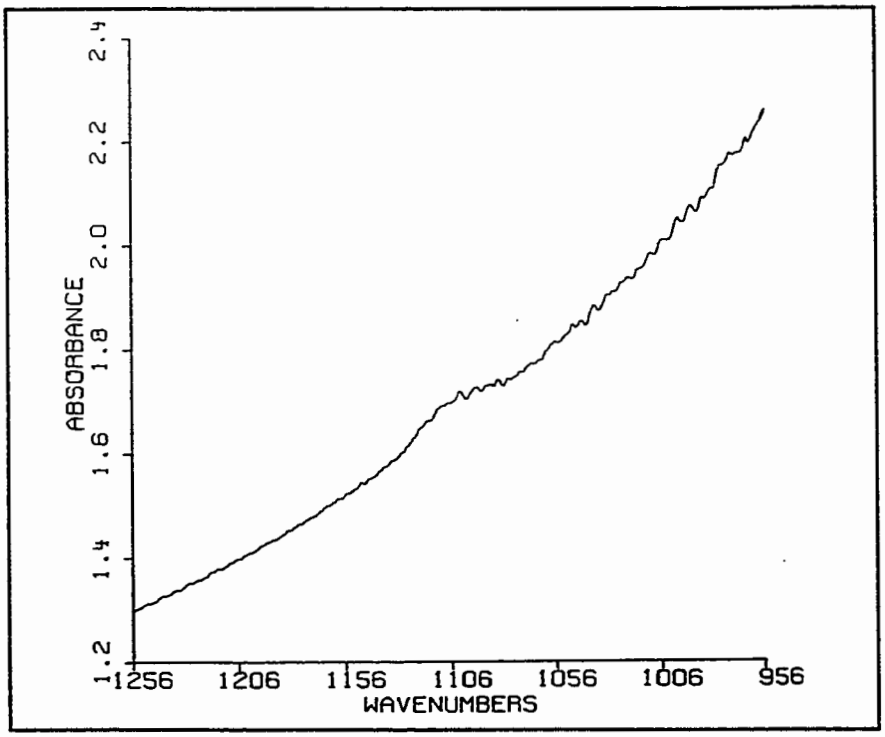

Figure 11. Spectrum of 0.019 ohm-cm (N_D = 1.5 x 10^{18} cm^{-3}) 410 microns thick antimony-doped silicon corresponding to the single beam spectra of Figure 10.

Since free carrier absorption increases with the dopant concentration N_D (21), the S/N for heavily doped silicon is reduced to the degree that the noise becomes the principal source of measurement error. Weeks (21) demonstrated this dependence of precision on dopant concentration by showing that the relative standard deviation of repeated oxygen measurements increases sharply for *n*-type resistivities below 0.1 ohm-cm (N_D = 7.8 x 10^{16} cm^{-3}). The degradation

of the S/N in low resistivity material has led to a wide acceptance that sufficiently precise infrared oxygen measurements require *n*-type resistivities greater than 0.1 ohm-cm ($N_D < 7.8 \times 10^{16}$ cm^{-3}) for 2 to 4 mm thick samples (6,15) or 0.05 ohm-cm ($N_D < 2.4 \times 10^{17}$ cm^{-3}) for wafers of approximately 500 microns thick (21). These restrictions exclude from consideration the commercially and technically interesting heavily doped *n*-type silicon used to produce epitaxial wafers, which typically have resistivities less than 0.04 ohm-cm ($N_D > 3.5 \times 10^{17}$ cm^{-3}).

In addition to the problems with measurement precision, the accuracy of oxygen measurements is affected by the free carrier absorption. The magnitude of this absorption is strongly dependent on both wavelength and resistivity. The wavelength dependence causes curvature of the spectrum which complicates the construction of the baseline from which peak height measurements are made (21). The resistivity dependence presents the practical difficulty of obtaining float zone references with resistivities closely matching those of the sample. Such references are required by the standard measurement technique (17) to subtract out the free carrier and lattice absorption spectra and to provide for the proper treatment of multiple reflections.

The following sections of this chapter systematically address these measurement problems. Section 3.1 establishes the limit for IR measurements as a function of noise level, signal intensity, precision requirements, and free carrier absorption. This limit relationship establishes an optimal sample thickness. A procedure is given for measurement of the spectral noise σ_s. Section 3.2 develops

a procedure for characterizing and optimizing the FTIR spectrometer in order to achieve maximum S/N. The final section presents a baseline correction technique which avoids the necessity of closely matched float zone references. Taken together, this work extends the range of applicability of the FTIR oxygen measurement technique beyond previously assumed limits.

3.1 NOISE AND THE LIMITS OF IR MEASUREMENT

The noise present in a transmittance or absorption spectrum is the result of noise contributions from both the background and sample spectra. The sample single-beam spectrum S and the background single-beam spectrum B may be represented as the sum of a signal spectrum and a pure noise spectrum:

$$S(\nu) = S_0(\nu) + S_n(\nu)$$

$$B(\nu) = B_0(\nu) + B_n(\nu)$$

$S_0(\nu)$ and $B_0(\nu)$ represent noiseless single beam spectra. The terms $S_n(\nu)$ and $B_n(\nu)$ represent noise spectra with zero average values and sample standard deviations of σ_s and σ_b respectively. As will be shown in Section 3.2, σ_s and σ_b will in general be different when the spectra are collected using different amplifier gains. In the above representation, the noise spectra $S_n(\nu)$ and $B_n(\nu)$ are assumed to be independent of the signal magnitudes $S_0(\nu)$ and $B_0(\nu)$. The data in Table

II supports this assumption. In this manner the noise has the characteristic of Johnson noise (22), which is independent of signal intensity.

TABLE II

SIGNAL AT 1105 CM^{-1}, AVERAGE VALUE OF 8 NOISE STANDARD DEVIATION MEASUREMENTS, STANDARD DEVIATION OF THE 8 MEASUREMENTS.

Signal	Avg σ	s.d.
1.85×10^{-2}	9.50×10^{-6}	9.47×10^{-7}
1.61×10^{-3}	8.70×10^{-6}	7.31×10^{-7}
1.56×10^{-4}	8.84×10^{-6}	1.12×10^{-6}

The sample transmittance spectrum T is given by the ratio of $S(\nu)$ to $B(\nu)$:

$$T = \frac{S_0(\nu) + S_n(\nu)}{B_0(\nu) + B_n(\nu)}$$

$$= \frac{1}{B_0(\nu)} \cdot \frac{S_0(\nu) + S_n(\nu)}{1 + (B_n(\nu)/B_0(\nu))}$$

Typically for FTIR equipment in good condition $(B_n(\nu)/B_0(\nu)) < 10^{-3}$. Dropping the explicit wavenumber dependence and using the approximation $(1 + B_n/B_0)^{-1} = 1 - B_n/B_0$ gives:

$$T = \frac{(S_0 + S_n)(1 - (B_n/B_0))}{B_0}$$

$$= \frac{S_0}{B_0} + \frac{S_n}{B_0} - \frac{S_0 B_n}{B_0^2} - \frac{S_n B_n}{B_0^2} \qquad 3.1$$

We can drop the term involving S_nB_n since it is negligible compared to the remaining terms. If the sample spectrum is acquired under the same conditions as the background spectrum, then $S_0 = B_0$ and we have the "100% line spectrum" T_{100}.

$$T_{100} = 1 + (S_n - B_n)/S_0 \qquad 3.2$$

Since the noise spectra in this case have the same standard deviation and add stochastically, the standard deviation of T_{100} has the value $2^{1/2}(\sigma_s/S_0)$. Note that even if σ_s is constant, the standard deviation of T_{100} has a frequency dependence since S_0 varies with frequency.

For the measurement of heavily doped silicon, the samples have a transmittance $(S_0/B_0) < 0.18$ [3], allowing us to drop the S_0B_n/B_0^2 term. Equation 3.1 becomes:

$$T = \frac{S_0}{B_0}\left(1 + \frac{S_n}{S_0}\right) \qquad 3.3$$

The noise of the transmittance spectrum is now determined solely by the noise level of the sample single beam spectrum. This is of practical importance for spectrometer optimization. If we are unable to simultaneously minimize the noise of both the open-beam spectrum and the sample spectrum, our efforts are best directed toward minimizing the sample noise.

---

[3]The value 0.18 is obtained from equation 3.8 by using the optimal thickness derived later.

Taking the $-\log_{10}$ of both sides of equation 3.3 to represent it in absorbance units:

$$-\log_{10} T = -\log_{10}(S_0/B_0) - \log_{10}(1 + (S_n/S_0))$$

$$= -2.30 \ln(S_0/B_0) - 2.30 \ln(1+(S_n/S_0))$$

Using the approximation $\ln(1+S_n/S_0) = S_n/S_0$ yields

$$-\log_{10} T = -2.30 \ln(S_0/B_0) - 2.30 (S_n/S_0) \qquad 3.4$$

For heavily doped silicon of thickness d, the noiseless transmittance $T_0 = S_0/B_0$ is given by

$$T_0 = S_0/B_0 = (1-R)^2 e^{-(\alpha(ox) + \alpha(el) + \alpha(l))d} \qquad 3.5$$

The α(ox), α(el), and α(l) are the absorption coefficients for interstitial oxygen, free carrier absorption, and intrinsic lattice absorption respectively. Equation 3.5 neglects the effect of multiple reflections, which are negligible in heavily doped material[4]. Substituting 3.5 into 3.4 and rearranging gives

$$-\log_{10}T + \log_{10}((1-R)^2 e^{-\alpha(l)d}) - \alpha(el)d) = 2.30\alpha(ox)d - 2.30(S_n/S_0) \qquad 3.6$$

The left-hand side of 3.6 represents the sample absorption spectrum after subtraction of both a noiseless float zone reference absorption spectrum to remove the intrinsic lattice spectrum and a noiseless free carrier absorption spectrum. The idealization of noiseless float zone and free carrier absorption spectra is closely approached in practice by using a computer-generated free carrier absorption spectrum and by averaging a large number of scans for the float zone spectrum.

---

[4]Proven in section 3.3.

The average and standard deviation of equation 3.6 gives an average value of the peak absorbance of $2.30\alpha(ox)d$ with a standard deviation of $2.30\sigma_s/S_0$. If the error in the peak absorbance is the principal cause of variation in the peak height measurement then the standard deviation of successive peak height measurements made on the same sample should equal $2.30\sigma_s/S_0$. This is equivalent to ignoring the effect of noise for determining the position of the baseline. The precision requirement of the experiment sets a maximum allowable value for the relative standard deviation M, so that for all acceptable measurements:

$$M \geq \frac{(2.30\sigma_s/S_0)}{2.30\alpha(ox)d}$$

Using $S_0 = B_0T$ and rearranging gives

$$\alpha(ox)d \geq \sigma_s/MB_0T \qquad 3.7$$

At 1105 cm^{-1} for *n*-type silicon below .040 ohm-cm ($N_D > 3.5 \times 10^{17}$ cm^{-3}), $\alpha(el) > 22$ cm^{-1}, $\alpha(l) = 0.8$ cm^{-1} and $\alpha(ox)$ is typically less than 4 cm^{-1}. We can then approximate equation 3.5 by

$$T_0 = (1-R)^2e^{-\alpha(el)d} \qquad 3.8$$

Substituting 3.8 into equation 3.7 gives

$$\alpha(ox) \geq \frac{\sigma_s}{MB_0(1-R)^2}\ [e^{\alpha(el)d}/d] \qquad 3.9$$

Equation 3.9 gives the minimum oxygen absorption coefficient and hence the minimum oxygen concentration which can be measured with an acceptable precision. There is an optimal value d which will minimize the value of equation 3.9. If we assume σ_s to be constant the minimum value of equation 3.9 is attained when:

$$d = d_{opt} = \alpha(el)^{-1}$$

The behavior of the function F in brackets in equation 3.9 is shown in Figure 12. The function increases relatively slowly away from its minimum so that small variations of the sample thickness from the optimal value do not seriously degrade the minimum measurable oxygen concentration.

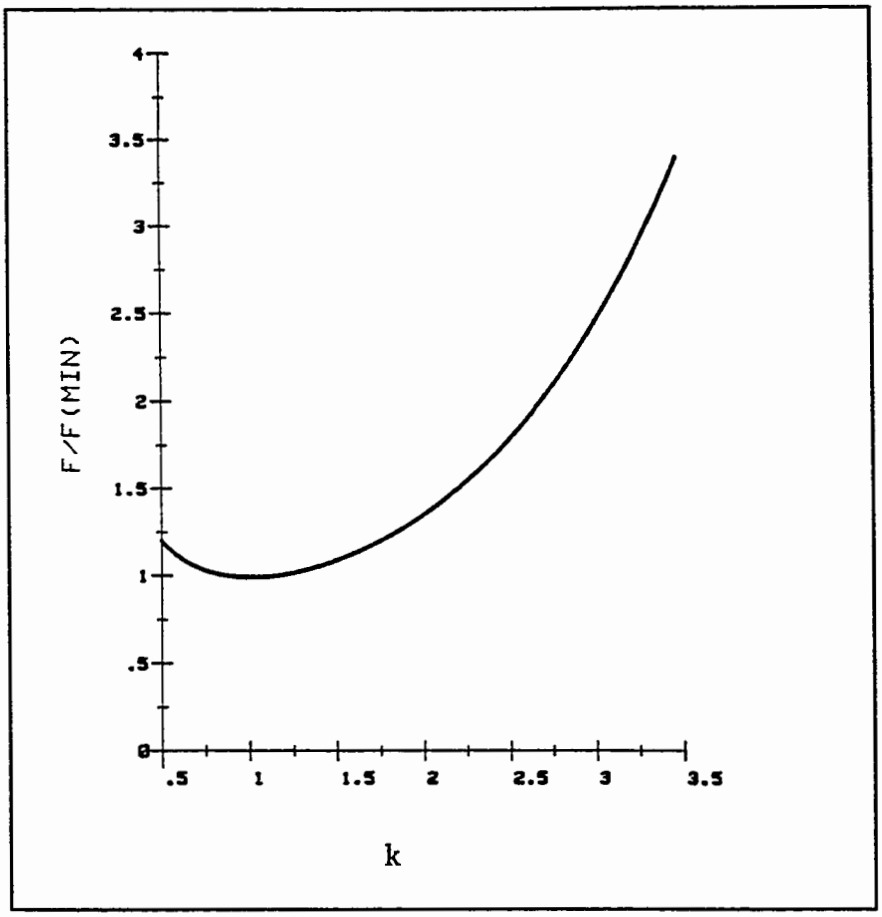

Figure 12. Plot of $F = (\alpha(el)e^{k})k^{-1}$ vs k where $k = \alpha(el)d$ and the function is normalized by its minimum value attained at $d = d_{opt}$.

At d_{opt}, the minimum measurable oxygen absorption coefficient is

$$\alpha(ox) = \frac{\sigma_s \alpha(el)e}{MB_0(1-R)^2} \qquad 3.10$$

A transmittance of 0.18 is obtained from equation 3.8 using $d = d_{opt}$ and $(1-R)^2 = 0.49$. This value differs from the well-known value of 0.38 established by ultraviolet-visible spectrophotometry (23) to provide the optimal S/N. Equation

3.8 shows that T = 0.38 requires $\alpha(el)d = 0.254$. Substitution of this value into the function F of Figure 12 yields $F \approx 5$, predicting that the conventional optimal value of T = 0.38 would actually give a five-fold degradation of the minimum measurable oxygen absorption coefficient compared to measurements made at T = 0.18. The difference is due to the $(1-R)^2$ factor. While a transmittance of 0.38 yields the optimal S/N for determination of absorbance, a value of 0.18 yields the optimal S/N for determination of the absorption coefficient $\alpha(ox)$.

The above analysis assumes that σ_s does not change as the sample thickness is reduced. In fact, σ_s increases when the FTIR amplifier gain decreases (see σ_s/G_2 in Table IV). The magnitude of the increase depends on the spectrometer characteristics. For a given transmittance there is a maximum gain which can be used while keeping the peak voltages of the interferogram within the range of the analog-to-digital converter. As the sample thickness d is decreased, the interferogram peak voltages increase and the maximum usable gain decreases. In some cases the proportional increase of the function F due to the use of a sample thickness $d_1 > d_{opt}$ is offset by the larger proportional decrease of σ_s due to the use of a larger gain. Then the minimum measurable oxygen absorption coefficient is achieved by use of the larger thickness d_1. For silicon measurements on the spectrometer used for this research the maximum possible advantage of using the higher gain is a factor of 1.2 for changes between a gain of 2 and a gain of 4.

Since 1.2 is a relatively small factor, use of d_{opt} for sample thickness instead of the true optimal thickness d_l will not substantially alter the measurement capabilities predicted by equation 3.10.

Use of equation 3.10 to predict the lowest measurable oxygen concentration, necessitates an accurate method for experimentally obtaining the spectral noise standard deviation σ_s. The general practice (24) for determining the noise is to calculate the standard deviation of the 100% line obtained by ratioing successive single beam spectra acquired under identical conditions. As mentioned previously, this standard deviation equals $2^{1/2}\sigma_s/S_0$. This method has the disadvantage of giving the S/N instead of σ_s. The noise calculations in this study use the method developed by Carter (25). In this method successive single beam spectra are subtracted. The signal, the same in each spectra, is eliminated leaving only the sum of two pure noise spectra. These noise spectra add stochastically, yielding a final pure noise spectrum with a standard deviation $2^{1/2}\sigma$ where σ is the standard deviation of the noise of either single spectrum.

The method for calculation of the standard deviation of the noise spectrum must be designed to separate out erroneous contributions due to baseline drift or distortion. By calculating the standard deviation from successive differences, the effect of such distortion of the noise spectrum on the calculated standard deviation is minimized (26). Using X_i as the i^{th} data point of the single beam

difference spectrum, the formula is.

$$\sigma = \left[\left(\sum_{i=1}^{N-1}(X_{i+1}-X_i)^2\right)/(2(N-1))\right]^{1/2} \qquad 3.11$$

where N is the number of data points in the measured spectral region.

A FORTRAN program written for the NICOLET™ *6000* FTIR data processing computer performed all of the noise calculations presented in this dissertation. This program reads the selected spectra from the mass storage medium, selects the data points corresponding to the wavenumber range of interest, performs the calculation of equation 3.11 over the specified wavenumber range, and outputs the standard deviation, the value of the single beam spectrum at a selected wavenumber and the ratio of these two values. A macro of FTIR commands was written to set the parameters used by the FORTRAN program and to collect the successive spectra used to calculate the noise. For this work, the noise data from 1006 to 1206 wavenumbers were used in the calculation and the value of the single beam spectrum was taken at 1105 wavenumbers. A sample of the program output and listings of the author's macro and FORTRAN program are in Appendix B.

Application of equation 3.11 to spectra which have been zero-filled involves a subtle point. The N-point spectra resulting from an interferogram of N_x points which was zero-filled to $N > N_x$ points prior to the Fourier transform has only N_x linearly independent points. The remaining $(N-N_x)$ points interpolate the spectra between the N_x independent data points (27). When using equation 3.11 for spectra with $N = 2N_x$, the interpolated data points reduce each $(X_{i+1} - X_i)$ term

by an average factor of 0.5. The calculated σ is then approximately half of the actual value. Increasing the amount of zero filling will further reduce the calculated σ. The effect of zero-filling is shown in Figure 13. Two 4096 successively acquired point interferograms were both zero filled to 8192 points prior to the Fourier transform. They were then subtracted to yield a pure noise spectrum. Application of 3.11 to the region 1206 to 1006 wavenumbers yielded a σ of 7.3×10^{-4}. The same two interferograms were processed again with zero filling to 16384 points instead of 8192 points. This yielded a σ of 3.9×10^{-4}. The additional zero filling reduced the computed σ to about half the previous value even though as can be seen from Figure 13 the peak-to-peak variation is nearly the same for both spectra. The value of σ can be empirically corrected for this effect by multiplying the value obtained from 3.11 by the factor (N/N_x).

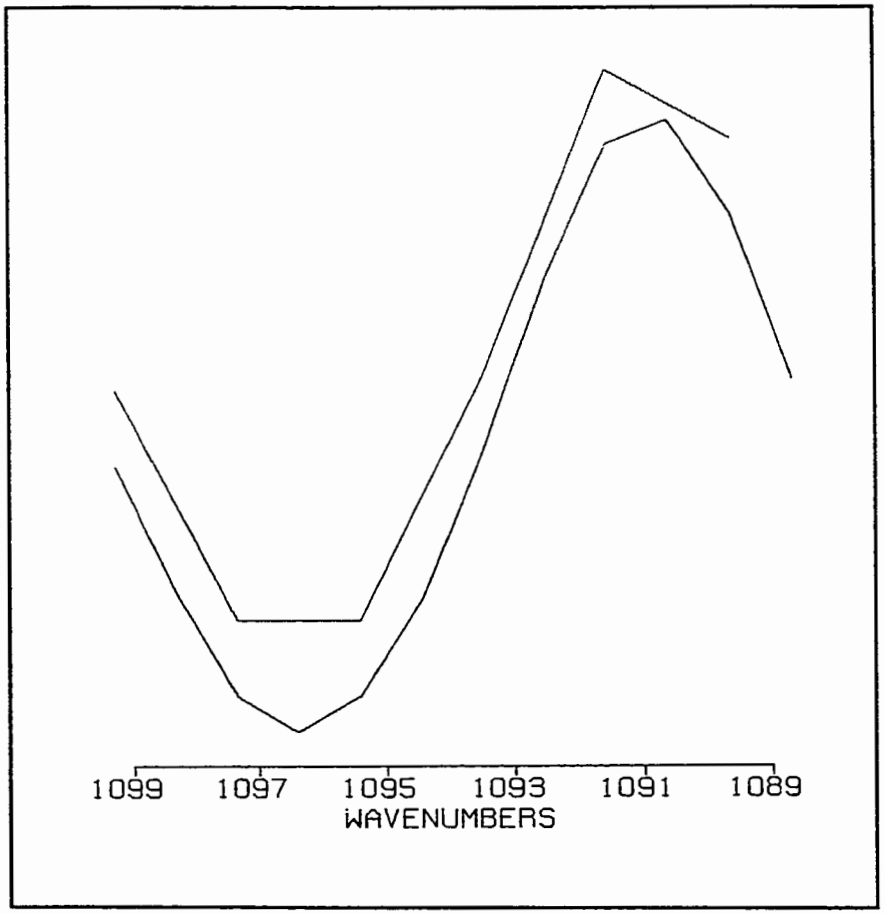

Figure 13. Noise spectra corresponding to 4096 point interferograms zero-filled to 8192 (top) or 16384 (bottom) data points. The spectra overlap but are offset for clarity.

Use of equation 3.10 to determine the practical limits of oxygen measurement requires knowledge of α(el) at 1105 cm^{-1} as a function of dopant concentration. Gladden (28) has compiled the published data from 3 sources for α(el) measured at 1000 cm^{-1} as a function of *n*-type dopant concentration. Over

the *n*-type dopant concentration range 2 x 10^{16} cm^{-3} to 1 x 10^{19} cm^{-3} these data fit a linear relationship. For α(el) in cm^{-1} and N_D in cm^{-3} this relationship is:

$$\log_{10}\alpha(el) = 1.23 \log_{10}(N_D/2.82 \times 10^{16}) \qquad 3.12$$

The variation of α(el) with wavenumber ν is given by (29)

$$\ln(\alpha(el)/N_D) = (m)\ln(\nu) + b \qquad 3.13$$

where m ≈ -2.0 and b ≈ -24.3.

Using 3.12 and 3.13 yields a relationship between α(el) at 1105 cm^{-1} and the *n*-type dopant concentration:

$$\log_{10}(\alpha_{1105}(el)) = 1.23 \log_{10}(N_D/3.32 \times 10^{16}) \qquad n\text{-type} \qquad 3.14$$

Similar calculations were done using Gladden's (28) *p*-type data over the dopant concentration range 4 x 10^{16} cm^{-3} to 1 x 10^{19} cm^{-3}. The result is:

$$\log_{10}(\alpha_{1105}(el)) = 1.15 \log_{10}(N_D/1.55 \times 10^{16}) \qquad p\text{-type}$$

These equations for α(el) provide a better fit to the experimental data of Gladden (28) than similar equations published by Pajot (15). Note that for a given dopant concentration, α(el) for *p*-type material is about double the α(el) for *n*-type material. For a given resistivity, the corresponding *p*-type dopant concentration is approximately 2 to 3 times the corresponding *n*-type dopant concentration (30). Thus for a given resistivity α(el) for *p*-type silicon is about 4 to 6 times α(el) for

n-type material. The large free carrier absorption coefficient α(el) for heavily doped *p*-type silicon makes IR measurements of interstitial oxygen in such material a practical impossibility.

An example may clarify the use of equation 3.10. Consider measurements in *n*-type silicon of optimal thickness d_{opt} with a resistivity of 0.023 ohm-cm (N_D = 1.0 x 10^{18} cm^{-3}). The acceptable error of the measurement is ±3% at 95% confidence level. The noise of the spectrometer is σ_s = 1 x 10^{-5} for a single scan of 4 cm^{-1} resolution. B_0 = 1.9 x 10^{-2} and a total of 128 scans will be signal averaged to yield the final spectrum. Then

$$M = .03/2 = .015$$

$$\sigma_s = 1.0 \times 10^{-5}/(128)^{1/2} = 8.8 \times 10^{-7}$$

From 3.14

$$\alpha_{1105}(\text{el}) = 66 \text{ cm}^{-1}$$

$$d_{opt} = \overset{-1}{\underset{1105}{\alpha}}(\text{el}) = 150 \text{ microns}$$

Substituting these values into 3.10 and[5] using R = 0.3 so $(1\text{-R})^2$ = .49 yields the minimum measurable oxygen absorption coefficient α(ox):

---

[5]R as a function of dopant concentration is given in Section 3.3.

$$\alpha(ox) = \frac{\sigma_s \alpha(el) e}{MB_0(1-R)^2} = \frac{(8.8 \times 10^{-7})(66)(2.7)}{(.015)(1.9 \times 10^{-2})(.49)}$$

$$= 1.1 \text{ cm}^{-1}$$

This corresponds to a minimum measurable oxygen concentration of 11 ppma (old ASTM). Since the oxygen concentration is typically in the range 20-40 ppma, quantitative measurements of this sample are well within the realm of possibility. This may be surprising given the resistivity limits for IR measurements cited in the first section of this chapter. There are several reasons for this superior measurement capability:

1. The spectrometer has been fully optimized for low transmittance samples by use of the techniques to be discussed in section 3.2.

2. The sample is much thinner than the 500 micron to 2 mm sample typically used for oxygen measurements.

3. The liquid nitrogen-cooled mercury-cadmium-telluride detector used for this research has an order of magnitude better S/N than the conventional DTGS pyroelectric detectors.

4. The number of scans averaged is larger than the 16 or 32 scans typically used for oxygen measurements.

Still further improvement is possible since, as will be proven in section 3.2, σ_s could be reduced by using 8 cm^{-1} or 16 cm^{-1} resolution. The value of σ_s could also be reduced by increasing the number of scans which are signal averaged. The improvement possible though signal averaging is limited by the long-term instrument drift which produces spectral distortions.

3.2 OPTIMIZATION OF THE FTIR SPECTROMETER

Equation 3.10 shows that the goal of equipment optimization for the measurement of heavily doped silicon is to minimize the ratio of σ_s /B_0. Note that this is not the typical S/N term since σ_s is determined from the sample spectrum and B_0 from the background spectrum. In a single-beam instrument such as an FTIR spectrometer, σ_s and B_0 are largely independent of each other and can be optimized separately.

The observed noise spectrum is generally the sum of noise spectra from several independent sources. The variance of the observed noise σ_s relates to the variance of the noise from the independent sources σ_i by

$$\sigma_s^2 = \sum_i \sigma_i^2 \qquad 3.15$$

By separating σ_s^2 into its component parts, we can identify the principal noise sources and choose parameters to minimize them. One procedure for this separation involves establishing conditions such that all terms in the sum in equation 3.15 are zero or negligible except for the single σ_i to be determined (31). Under these conditions $\sigma_s = \sigma_i$. Repeating this process using different conditions will successively yield the values of other variances. Unfortunately, isolating terms for FTIR spectrometers in the manner just described is not always

possible since the equipment or parameter changes required may alter the functioning of the instrument.

The following modification of the above procedure developed by the author for use with FTIR spectrometers determines the noise components while operating the instrument in the normal manner. The method requires that equation 3.15 be written in the form

$$\sigma_s^2 = \sum_i (G_i \sigma_i)^2 \qquad 3.16$$

where the value of G_i is determined by an easily modified FTIR equipment parameter. If we keep all factors G_i constant except for G_k then 3.16 can be written as

$$\sigma_s^2 = G_k^2 \, \sigma_k^2 + C \qquad 3.17$$

where C is the sum of all remaining $G_i^2 \sigma_i^2$ terms. Note that no assumptions have been made regarding the relative magnitudes of the terms. Using the noise measurement procedure described in Section 3.1 to obtain σ_s for several values of G_k , and plotting σ_s^2 versus G_k^2 will yield a straight line. The slope of the line equals σ_k^2 and the intercept equals C. Repeating this noise separation procedure determines the remaining σ_i terms. For purposes of using this technique to analyze the origins of the noise, the FTIR can be considered to consist of subsystems, each of which contributes to the total noise σ_s.

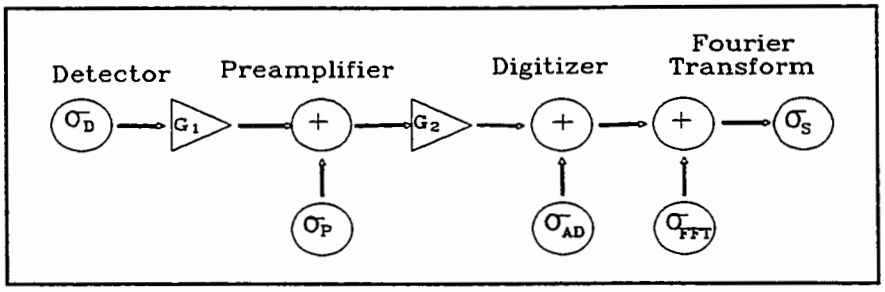

Figure 14. Schematic representation of the sources of noise in an FTIR spectrometer.

This is represented schematically in Figure 14 where σ_D, σ_P, σ_{AD} and σ_{fft} represent the standard deviation of noises contributed by the detector, preamplifier, digitizer and computation of the Fourier transform respectively. The G_1 and G_2 represent the gains of the amplifiers in the signal processing system. Gain G_1 is changed by manual adjustment of a potentiometer located on the preamplifier board mounted on the detector. Gain G_2 is changed via software using the GAN command.

Prior to the Fourier Transform, the noise refers to variation occurring in the time domain, while after the transform the noise refers to variation occurring in the frequency domain. The connection between the variances of the noise in these two domains is provided by Parseval's Relation for the N-point discrete Fourier Transform (32):

$$\sigma_s^2 \equiv [\sum_{k=0}^{N-1} | S_n(\nu_k)|^2]/N = \sum_{j=0}^{N-1} |V_n(j)|^2$$

In the above, $V_n(j)$ is the value of the noise component of the digitized

interferogram at the *j*th point. If additional computational noise is added during the calculation of the FFT the relationship becomes (33):

$$\sigma_s^2 = N(N^{-1} \sum_{j=0}^{N-1} | V_n(j) |^2) + \sigma_{fft}^2$$

or

$$\sigma_s^2 = N\sigma_v^2 + \sigma_{fft}^2 \qquad 3.18$$

Here σ_{fft}^2 is the variance of the noise added during calculation of the FFT and σ_v^2 is the variance of the noise of the digitized interferogram. From equation 3.15:

$$\sigma_v^2 = \sigma_d^2 + \sigma_p^2 + \sigma_{AD}^2$$

Equation 3.18 is of the form of equation 3.17 with the number N of transform points substituting for G_k^2 and with $C = \sigma_{fft}^2$. N can be varied in powers of two from 1024 using the software parameter NTP. To obtain data to test this model, two successive 8192 point interferograms were acquired and stored. Spectra obtained by transforming only the first N = 1024 points of the stored interferograms were subtracted to provide the noise spectra used to calculate σ_s. This process was repeated for N = 2048, 4096 and 8192. Table III shows that average values for 20 such measurements. Applying this noise separation procedure to the data in Table III yields:

$\sigma_{fft}^2 = 1.13 \times 10^{-12}$

$\sigma_v^2 = 9.29 \times 10^{-15}$

$r^2 = 0.987$

TABLE III

NUMBER OF POINTS IN THE FOURIER TRANSFORM, AVERAGE OF 20 MEASUREMENTS OF σ_s.

N	AVG σ_S
1024	2.805×10^{-6}
2048	4.491×10^{-6}
4096	6.636×10^{-6}
8192	8.670×10^{-6}

For single scans with N = 4096 the value of $N\sigma_v^2$ is 3.8×10^{-11}. Since this is substantially larger than σ_{fft}, the observed spectral noise is primarily due to the noise of the interferogram so $\sigma_s^2 \approx N\sigma_v^2$. This suggests that we can dramatically reduce σ_s^2 by using small values of N. There is a limit to the improvement achieved by this since reducing N degrades the resolution and will reduce the measured peak height when the resolution is comparable to the peak width (34).

To visually show the effect of varying N on noise, the interferograms of length 1024, 2048, 4096 and 8192 were zero-filled to 8192 points and then transformed. This provided for the same data point spacing for all spectra. These

spectra are in Figure 15 and clearly show the increase in noise with increases of N.

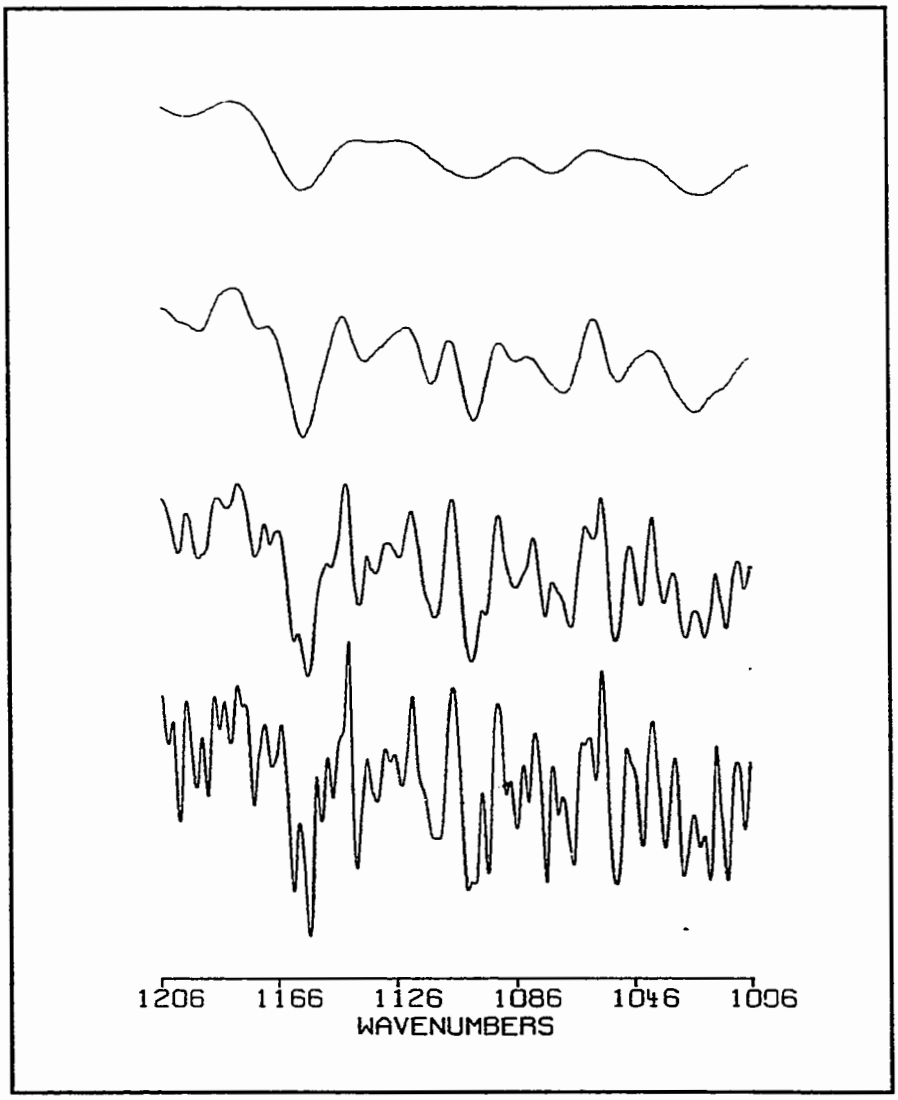

Figure 15. Spectra for 1024, 2048, 4096 and 8192 point interferograms showing the effect of N on noise.

Keeping N fixed we can further reduce σ_s^2 by reducing σ_v^2. Referring to Figure 14, we can write σ_s^2 as

$$\sigma_s^2 = N\sigma_v^2 = N(\sigma_{AD}^2 + G_2^2(\sigma_p^2 + G_1^2\sigma_D^2)) \qquad 3.19$$

We have dropped σ_{fft}^2 since for N > 1024, $N\sigma_v^2 >> \sigma_{fft}^2$. Defining

$$N\sigma^2 = \sigma^{*2}$$

equation 3.19 becomes:

$$\sigma_s^2 = \sigma_{AD}^{*2} + G_2^2(\sigma_p^{*2} + G_1^2\sigma_D^{*2}) \qquad 3.20$$

Table IV presents measurements of σ_s from an experiment where G_2 was varied while G_1 was held constant. The average σ_s is taken over 20 measurements. The apparent increase of σ_s with increasing gain G_2 can be misleading. Prior to ratioing the single-beam spectra to obtain the transmittance, the single-beam spectra are divided by their respective G_2 values. The standard deviation of the noise of the spectrum is then given by σ_s/G_2 As shown by the entries in Table IV for σ_s/G_2, the noise of a spectrum will decrease as G_2 is increased.

TABLE IV

MEASUREMENT OF σ_s WITH G_1 HELD CONSTANT, G_2 VARIABLE.

G2	Avg σ_s	σ_s/G_2
1	6.645×10^{-6}	6.645×10^{-6}
2	9.000×10^{-6}	4.500×10^{-6}
4	1.512×10^{-5}	3.780×10^{-6}

A linear regression of σ_s^2 versus G_2^2 using the data in Table IV yields:

$$(\sigma_p^{*2} + G_1^2\sigma_D^{*2}) = 1.23 \times 10^{-11}$$

$$\sigma_{AD}^{*2} = 3.18 \times 10^{-11}$$

$$r^2 = 1.000$$

The data above shows that for $G_2 = 1$ (the value used for collecting the open-beam background spectra) the noise due to the digitizer exceeds the noise due to the detector and preamplifier. Under these conditions any reductions in the detector or preamplifier noise has a negligible effect on σ_s^2. This suggests that whenever possible optimization studies or experiments should be performed at amplifier gains $G_2 \geq 2$.

The next phase of this study was to optimize σ_p^* and σ_D^*. With a small aperture in the beam the signal intensity was reduced so that a gain of $G_2 = 4$ could be used without exceeding the voltage range of the digitizer. Under these

conditions σ_{AD}^{*} would be neglected so equation 3.20 becomes:

$$\sigma_s^2 = 16(\sigma_p^{*2} + G_1^2\sigma_D^{*2}) \qquad 3.21$$

The noise produced by mercury-cadmium-telluride detectors is a function of the bias current I_B. Table V gives measurements of σ_s^2/S(1105) for several bias currents. The term S(1105) is the value of the single beam spectrum at 1105 cm^{-1}.

TABLE V

BIAS CURRENT I_B, AVERAGE OF 8 MEASUREMENTS OF σ_s, SPECTRUM AT 1105 CM^{-1} S(1105) AND THE S/N S(1105)/σ_s.

I_B(ma)	AVG σ_s	S(1105)	S/N
16.0	9.2×10^{-5}	.0137	149
12.0	6.2×10^{-5}	.0099	160
10.0	4.8×10^{-5}	.0082	173
8.0	3.7×10^{-5}	.0066	176
6.0	2.9×10^{-5}	.0050	175
4.0	2.1×10^{-5}	.0034	158
2.0	2.1×10^{-5}	.0017	84

The S/N reaches a maximum value between 6 and 10 ma. The FTIR as supplied by the manufacturer had I_B = 20 ma. Carter (25) had similarly determined that the optimal S/N occurred for I_B values well below the manufacturers recommendations.

To determine σ_p^* and σ_D^* from equation 3.21, σ_s was measured as a function of G_1. G_1 was determined by ratioing the values of S(1105). The data from this experiment is shown in Table VI.

TABLE VI

EFFECTIVE GAIN G_1, AVERAGE OF 8 MEASUREMENTS OF σ_s.

G_1	AVG σ_s
0.602	1.543×10^{-5}
1.000	1.797×10^{-5}
1.265	2.171×10^{-5}
1.524	2.367×10^{-5}
1.820	2.670×10^{-5}
1.939	2.720×10^{-5}

A linear regression of σ_s^2 versus G_1^2 yields:

$$\sigma_p^* = 1.39 \times 10^{-5}$$

$$\sigma_D^* = 1.24 \times 10^{-5}$$

$$r^2 = .986$$

Figure 16 shows a plot and regression line for σ_s^2 versus G_1^2 using the data from Table VI.

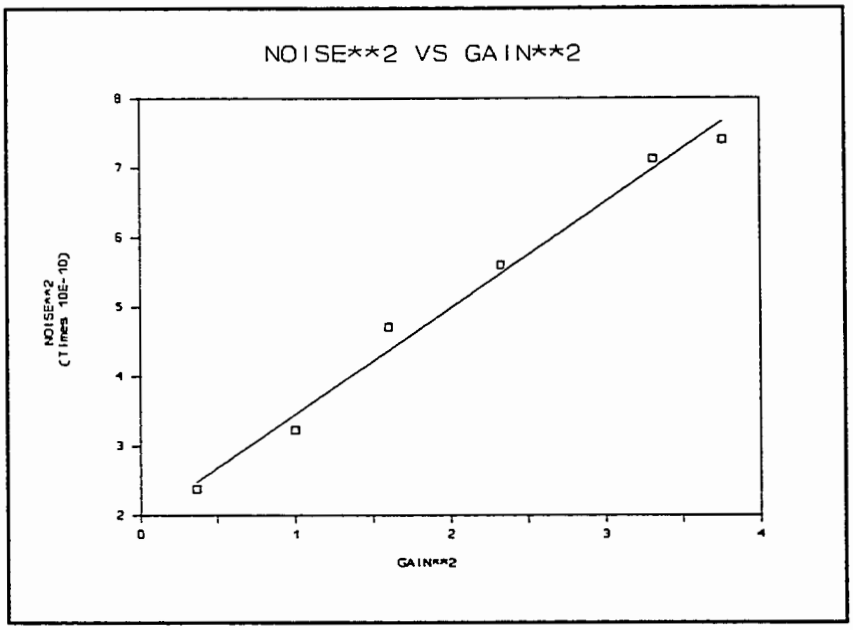

Figure 16. Graph of the data and regression line used to determine σ_D^* and σ_p^*.

Note that for values of $G_1 \leq 1$ the noise is largely determined by the preamplifier noise σ_p^*. It would be desirable to increase $G_1 > 1$ so that the detector noise would be the primary contributor to σ_s. Unfortunately, values of $G_1 > .6$ would result in peak-to-peak voltages of the interferogram exceeding the voltage limits of the digitizer.

Use of the adjustable bandwidth filters prior to the digitizer input allowed us to overcome this limitation. All frequencies in the spectrum contribute to the height of the interferogram peak, yet it is only a narrow range of frequencies which are of interest for semiconductor measurements. By adjusting the low pass

filter using parameter LPS the frequencies outside the range of interest are attenuated, thereby reducing the peak-to-peak voltage of interferogram signal. The frequency response of the filter is shown in Figure 17. Figure 17 was obtained by ratioing an open-beam background scanned with the filter on to a background scanned with the filter off. Note that the transmittance in the region around 1105 cm^{-1} is nearly 100% while higher frequencies are strongly attenuated. This allowed the use of larger gains G_1 which improve the S/N ratio. The use of the above techniques for the optimization of the FTIR spectrometer improved the S/N by an approximate factor of 5 to 7.

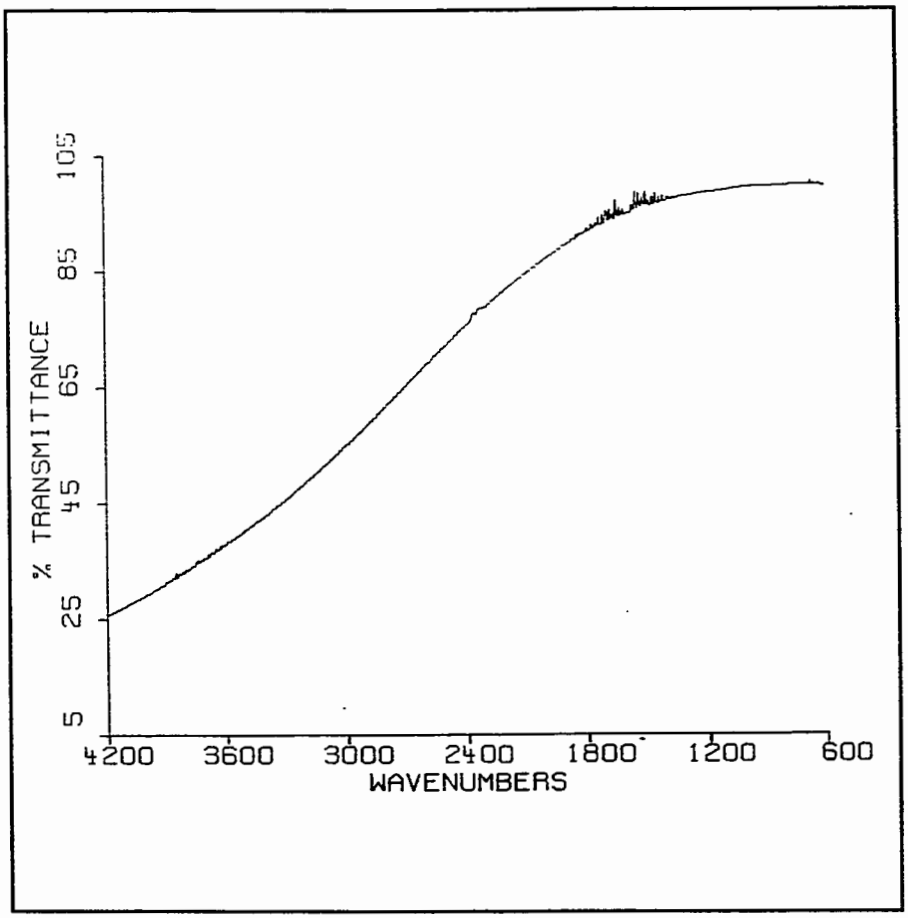

Figure 17. Frequency response of filter used to reduce interferogram peak-to-peak voltage.

3.3 MEASUREMENT PROCEDURE

Interstitial oxygen measurements using the difference method (6) require subtraction of a float zone reference spectrum from the sample spectrum prior to measurement of the 1105 cm^{-1} peak height. The procedure requires that all absorption bands except for the interstitial oxygen band at 1105 cm^{-1} be identical

in sample and reference. For heavily doped silicon this procedure has the following disadvantages:

1. The rapid change of α(el) with resistivity would necessitate a large number of float zone references to match samples which span the *n*-type resistivity range 0.015 ohm-cm (N_D = 2.2 x 10^{18} cm^{-3}) to 0.040 ohm-cm (N_D = 3.5 x 10^{17} cm^{-3}).

2. Heavily doped float zone silicon is not readily available.

3. A heavily doped float zone reference spectrum will have a S/N similar to that of the sample spectrum. The noise on the float zone spectrum adds stochastically to the noise of the sample spectrum, resulting in a degradation of the S/N by a factor of $2^{-1/2}$.

These problems are overcome through use of a computer-generated free carrier absorption spectrum in conjunction with a high resistivity float zone reference. The synthetic spectrum can be generated for any resistivity and subtracts out the free carrier absorption band of the sample without introducing additional noise. The high resistivity float zone reference is then used only to subtract out the intrinsic lattice absorption bands. The successive subtractions of a free carrier absorption spectrum and a float zone spectrum correspond to the operation represented in the left-hand side of equation 3.6.

The initial approach taken to the generation of the free carrier absorption spectrum followed Weeks (21). The complex index of refraction n(ν) was calculated for a given resistivity from Maxwell's equations using a Drude model for the conductivity (35). The absorption coefficient α(el) for light with a

vacuum wavelength of L_0 is then given by:

$$\alpha(el) = 4\pi n_i(\nu)/L_0 \qquad 3.22$$

where the extinction coefficient $n_i(\nu)$ is the imaginary part of $n(\nu)$. Using the values for $\alpha(el)$ from equation 3.22, the free carrier absorption spectrum A is calculated from equations 3.23:

$$A = -\log_{10}(T_0)$$

$$T_0 = (1-R)^2 e^{-\alpha(el)d}/(1-R^2 e^{-2\alpha(el)d}) \qquad 3.23$$

The Fortran program *NPLUS.ASC* written for the NICOLET^{tm} *6000* FTIR data processing computer performed the calculation of $n(\nu)$ and then computed the free carrier absorption spectrum using equations 3.22 and 3.23. A listing of the program is in the Appendix C. The absorption spectrum obtained from this program agreed in shape but differed in magnitude from experimentally obtained free carrier absorption spectra. Obtaining a good match between the actual and calculated spectra required considerable trial-and-error adjustment of the resistivity and thickness values input into the program. However, the match is more easily obtained by generating a synthetic spectrum calculated using arbitrary values for resistivity and thickness, determining a factor FCR which eliminates curvatures of the spectrum due to free carrier absorption, and then multiplying the spectrum by that factor. On the NICOLET^{tm} *6000* the determination of an appropriate FCR is facilitated by an interactive display which shows the result of subtracting (FCR x Synthetic spectrum) from the sample spectrum as FCR is varied. An

approximation of equation 3.22 for the wavelength and carrier concentration range we are using provides support for this empirical procedure

$$\alpha(\text{el}) \approx (4\pi N_D e^2/3.42cm^*)(\tau//(1 + w^2\tau^2) \qquad 3.24$$

Here e is the charge of the electron, c is the speed of light, τ is the Drude relaxation time, w is the angular frequency of the radiation and m^* is the effective mass for electrons in the conduction band. For *n*-type resistivities greater than 0.020 ohm-cm, $w\tau > 6$ so equation 3.24 can be simplified to:

$$\alpha(\text{el}) \approx (4\pi Ne^2/3.42c)(N_D/\tau m^*)(1/w^2) \qquad 3.25$$

Multiplying the synthetic spectrum by FCR is equivalent to changing the value of the term $(N_D/\tau m^*)$ in equation 3.25.

Gladden (28) eliminated the free carrier absorption by subtracting from the sample spectrum a synthetic spectrum calculated using equation 3.13. The parameters m and b were calculated in each case to provide the best fit of the synthetic spectrum to the sample spectrum over the ranges 1033-1200 cm^{-1} and 1060-1000 cm^{-1}. The interactive procedure used for this research is preferred since it allows the operator to visually account for precipitate bands in the range 1300-1000 cm^{-1} which could affect the calculations of the parameters m and b.

After elimination of the free carrier absorption, a lightly doped float zone reference is subtracted from the sample to eliminate the silicon lattice absorption bands. Because of the difference between the absorbance of the float zone

reference and the sample, special attention must be given to the treatment of the multiple reflection correction (MRC) discussed in Chapter II. The float zone reference is corrected using the program MRC discussed previously. Use of this program requires accurate values for transmittance. To minimize photometric inaccuracies due to the nonlinear detector/amplifier response, the float zone reference was measured after inserting an aperture in the beam. This aperture reduced the open beam light intensity, allowing the detector to operate in its linear response region, where it is capable of providing accurate transmittance values.

Performing the MRC for the sample requires a different approach. Here the reduction in S/N caused by the aperture is unacceptable. Use of the effective thickness correction method discussed in Chapter II avoids this difficulty. The peak height H in absorbance units is measured on the sample spectrum obtained without using the aperture. This sample has a high S/N, but possibly poor photometric accuracy. A second sample spectrum is scanned, with the aperture in place. This spectrum has good photometric accuracy, but possibly a poor S/N. The accurate value for transmittance at 1105 cm^{-1} obtained from this second spectrum is substituted into equation 2.11c to obtain g. The oxygen absorption coefficient is then given by equation 2.10:

$$\alpha(ox) = 2.303H/(d(1+g))$$

The effect of MRC for heavily doped material is small but not insignificant. Considering samples with the optimal thickness d_{opt}, substitution of $\alpha d = 1$ into equation 2.3 and 2.11b shows that while the multiple reflections increase the transmittance by only 1.2%, they change the observed peak height by 2.5%.

In this chapter, it was assumed that the reflectance R = 0.3 regardless of dopant concentration. The reflectance can be derived from the complex index of refraction $n(\nu)$ discussed earlier:

$$R = ((1 - n_r)^2 + n_i^2)/((1 + n_r)^2 + n_i^2) \qquad 3.25$$

where n_r is the real part of $n(\nu)$. Senitzky and Weeks (35) show that the reflectance calculated using 3.25 is in good agreement with experiment. Figure 18 shows the calculated relationship between reflectance and dopant concentration for *n*-type silicon. For dopant concentrations less than 3×10^{18} cm^{-3} we can use R = 0.30 without incurring errors greater than 0.2%.

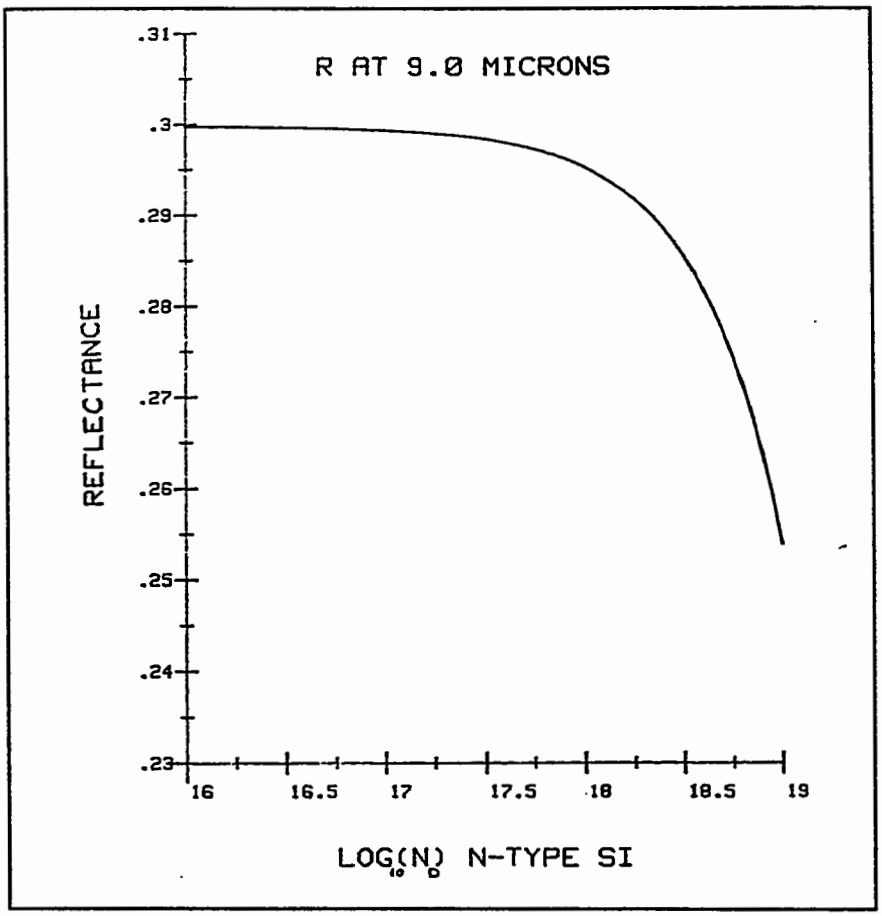

Figure 18. Reflectance as a function of dopant concentration.

CHAPTER IV

THE ROLE OF POINT DEFECTS IN THE NUCLEATION AND PRECIPITATION OF OXYGEN IN SILICON.

Point defects are believed to play important roles in diffusion (36,37,38), oxidation (39) and nucleation/precipitation processes (40,41) in silicon. There is disagreement as to whether silicon interstitials are required to explain the observed phenomena (42). Much of the literature uses models which assume that silicon interstitials are the primary defects mediating dopant diffusion and precipitation of oxygen in silicon. This is despite the fact that vacancies and vacancy complexes have been definitely identified in silicon using Electron Paramagnetic Resonance (43), Deep Level Transient Spectroscopy (43) and Positron-Lifetime (44) and silicon interstitials have never been observed with these techniques.

This chapter studies the nucleation/precipitation of oxygen in silicon with the assumption that vacancies are the primary point defects in silicon. Since vacancies have been experimentally determined to exist in several charge states, the total equilibrium concentrations of vacancies of all charge states is determined by the dopant concentration (45). A study of nucleation/precipitation as a

function of dopant concentration may help elucidate both the type and the role of the dominant point defect in silicon.

Section 4.1 reviews the thermodynamics of point defects in semiconductors. Particular attention is given to the equilibrium concentration of the various negatively charged (acceptor) vacancy states as a function of the location of the Fermi Level within the band gap. Only neutral and acceptor vacancy states are considered since the concentrations of positively charged (donor) vacancies are negligible in the cases considered in this work.

Section 4.2 presents a calculation method to determine the vacancy concentration in silicon as a function of temperature and dopant concentration. Unlike previous vacancy concentration calculations (39,46), this method considers both the neutral and negatively charged states of both vacancies and divacancies.

Section 4.3 reviews the theory of nucleation of oxygen precipitates and proposes a model to account for the observed decrease of nucleation/precipitation in heavily doped *n*-type silicon (47,48). This model allows quantitative prediction of the effect of dopant concentration on nucleation in terms of an equivalent reduction in the interstitial oxygen concentration. Unlike a similar qualitative explanation proposed by Hahn et al (49) this model does not require that the vacancy concentration be undersaturated. Other authors have proposed models using oxygen-vacancy pairs (48) or antimony-vacancy pairs (47) to account for the reduced precipitation in heavily doped *n*-type material. However, these authors have not provided quantitative calculations substantiating the effect of

such pairs at nucleation temperatures.

Section 4.4 presents experimental data from a study comparing nucleation/ precipitation in heavily doped and lightly doped silicon.

4.1 THERMODYNAMICS OF POINT DEFECTS

A system is in thermodynamic equilibrium with respect to the reaction

$$aA + bB \longleftrightarrow cC + dD$$

when (50)

$$a\mu(A) + b\mu(B) - c\mu(C) - d\mu(D) = 0 \qquad 4.1$$

In equation 4.1 $\mu(i)$ is the chemical potential of the species i. The chemical potential terms can be separated into a concentration-independent term $\mu^0(i)$ called the Standard Chemical Potential of i and a concentration-dependent entropy of mixing term (51):

$$\mu(i) = \mu^0(i) + kT \ln([i]/[Ni]) \qquad 4.2$$

where k is the Boltzmann constant, T is the Kelvin temperature, [i] is the concentration of i and [Ni] is the reference concentration for i. Substituting equation 4.2 into 4.1 yields the Law of Mass Action:

$$[A]^a [B]^b [C]^{-c} [D]^{-d} = K(T) \qquad 4.3a$$

$$K(T) = [N_A]^a [N_B]^b [N_C]^{-c} [N_D]^{-d} \exp(-\Delta \mu^0/kT) \qquad 4.3b$$

$$\Delta\mu^0 = a\mu^0(A) + b\mu^0(B) - c\mu^0(C) - d\mu^0(D) \qquad 4.3c$$

The term K(T) is the equilibrium constant and $\Delta\mu^0$ is the Standard Free Energy Change of the Reaction. The term $\Delta\mu^0$ can be separated (51) into a Standard Enthalpy Change ΔH^0 and a Standard Entropy Change ΔS^0.

$$\Delta\mu^0 = \Delta H^0 - T\Delta S^0 \qquad 4.4$$

The concentration of neutral vacancies V^x in silicon is determined by the reaction (51):

$$0 \longleftrightarrow V^x \qquad 4.5$$

Equation 4.5 represents the formation of a vacancy by moving a silicon atom from the interior of the crystal to the surface. Applying equations 4.2 - 4.4 to the above reaction yields:

$$[V^x] = N_L \exp(\Delta S^0/k) \exp(-\Delta H^0/kT) \qquad 4.6$$

N_L is the density of lattice sites in silicon 5.0×10^{22} cm^{-3}. Van Vechten (51) gives the values

$$\Delta S^0 = 3k$$

$$\Delta H^0 = 2.4 \text{ ev}$$

At a temperature of 750° C, equation 4.6 predicts a neutral vacancy concentration of 1.5×10^{12} cm^{-3}.

The neutral vacancies can react to form neutral divacancies V_2^x by the reaction (51):

$$V_2^x \longleftrightarrow V^x + V^x \qquad 4.7$$

$$\Delta S^0 = -(k)\ln(4)$$

$$\Delta H^0 = 1.7 \text{ ev}$$

Applying equations 4.2 - 4.4 to reaction 4.7 yields:

$$[V_2^x] = [V^x]^2 N_L^{-1} \, 4 \exp(1.7/kT) \qquad 4.8$$

In equation 4.8 concentrations are expressed in cm^{-3} and kT has units of electron volts (ev).

The vacancies and divacancies can also react with the electrons or holes in the semiconductor to form ionized defects. The reaction of a neutral vacancy with an electron from the conduction band to form an ionized vacancy V^- is represented by equation 4.9:

$$V^x + e^- \longleftrightarrow V^- \qquad 4.9$$

The chemical potential of the electrons in the conductor band is equal to the Fermi level E_F (52). Putting the reaction 4.9 into the form of equation 4.1 yields:

$$\mu^0(V^x) + kT \ln([V^x]/N_L) + E_F - \mu^0(V^-) - kT \ln([V^-]/2N_L) = 0 \qquad 4.10$$

The difference $\mu^0(V^-) - \mu^0(V^x)$ called the ionization level $E(V^-)$ is equal to the Standard Free Energy Change for the reaction of equation 4.9. Equation 4.10 becomes:

$$[V^-] = 2[V^x] \exp((E_F - E(V^-))/kT) \qquad 4.11$$

The factor of 2 in equation 4.11 is due to the two-fold degeneracy of V^- coming from occupancy by an electron with either spin up or spin down.

In a similar manner we can write equations for the concentration of doubly ionized vacancies V^{-2}, singly ionized divacancies V_2^-, and doubly ionized divacancies V_2^{-2}:

$$[V^{-2}] = 0.5[V^-] \exp((E_F - E(V^{-2}))/kT) \qquad 4.12$$

$$[V_2^-] = 2[V_2^x] \exp((E_F - E(V_2^-))/kT) \qquad 4.13$$

$$[V_2^{-2}] = 0.5[V_2^-] \exp((E_F - E(V_2^{-2}))/kT) \qquad 4.14$$

The same procedure can be used to obtain the concentration of ionized dopant atoms. For antimony (Sb) the ionization reaction and equivalent equation are:

$$Sb^x \longleftrightarrow Sb^+ + e^-$$

$$[Sb^+] = 2[Sb^x] \exp((E(Sb) - E_F)/kT) \qquad 4.15$$

$$E(Sb) = \mu^0(Sb) - \mu^0(Sb^+)$$

Using $[Sb^+] + [Sb^x] = N_D$ where N_D is the concentration of antimony dopant and solving for $[Sb^+]$ yields:

$$[S_b^+] = N_D/(1 + 0.5 \exp((E_F - E(Sb))/kT)) \qquad 4.16$$

The ionization levels for the above reactions are typically given pictorially by showing the energies of the levels relative to the conduction band energy E_c and valence band energy E_v. Figure 19 shows the ionization levels discussed above in that form for T = 0°K (51).

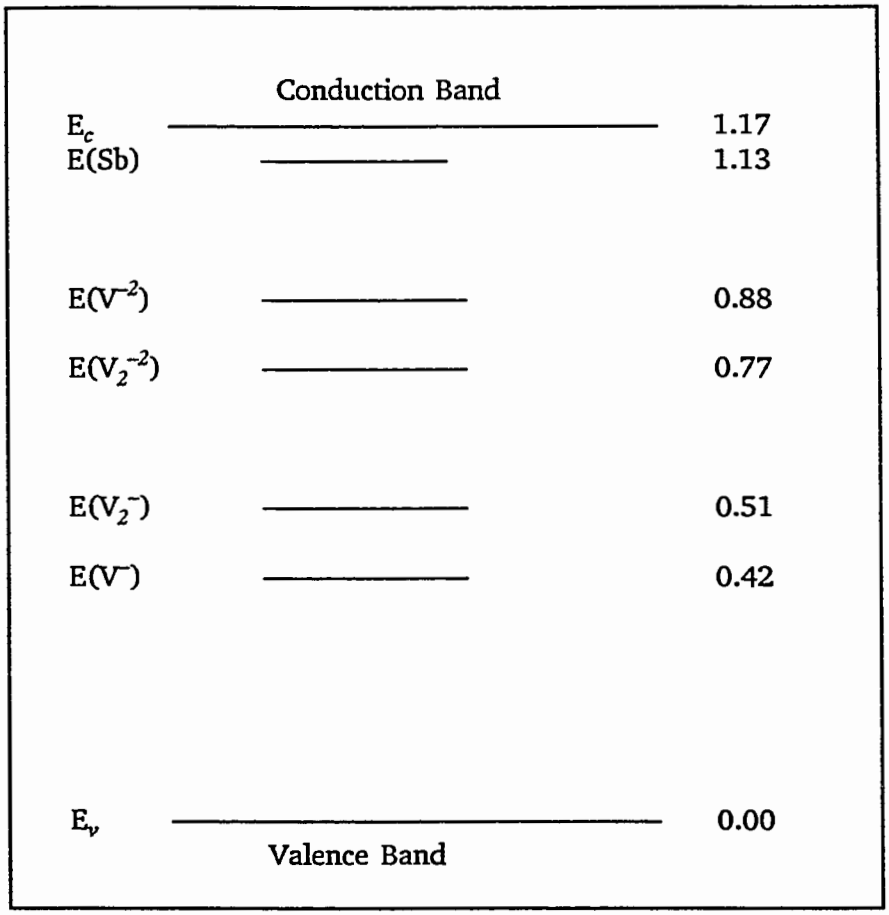

Figure 19. Ionization levels in electron volts for vacancies, divacancies and antimony in silicon at 0°K (51).

Equation 4.9 represents the reaction where a neutral vacancy captures an electron from the conduction band to become an ionized vacancy. This reaction could also be written to represent the emission of a hole (h^+) by the neutral vacancy into the valence band:

$$V^x \longleftrightarrow V^- + h^+ \qquad 4.9a$$

Both equation 4.9 and 4.9a are equivalent and lead to equation 4.10 since the

chemical potentials of electrons in the conduction band and holes in the valence band are related by (52):

$$\mu(e^-) = -\mu(h^+)$$

Note from equations 4.11 and 4.12 that when E_F is larger than the vacancy ionization levels $E(V^-)$ and $E(V^{-2})$ the equilibrium concentration of charged vacancies will exceed the concentration of neutral vacancies V^x. The same relation holds for divacancies. We can achieve a large value for E_F with a high *n*-type dopant concentration. In equilibrium the concentration of neutral vacancies and divacancies are functions of temperature and are independent of the dopant concentration. The total effective equilibrium vacancy concentration $[V_{TE}]$ is given by:

$$[V_{TE}] = [V^x] + [V^-] + [V^{-2}] + 2([V_2^x] + [V_2^-] + [V_2^{-2}]) \qquad 4.17$$

V_{TE} is a function of temperature and of dopant concentration. From the above discussion we expect that $[V_{TE}]$ will be much larger in heavily doped silicon than in lightly doped silicon. The following section presents a calculation procedure for $[V_{TE}]$ which confirms this prediction.

4.2 CALCULATION OF POINT DEFECT CONCENTRATIONS

Use of equations 4.11 - 4.15 to calculate ionized point defect concentrations requires the ionization levels given for T = 0°K in Figure 19 be extrapolated to the temperature of interest. Van Vechten (9) suggested that the change in the vacancy and divacancy ionization levels from 0°K to the temperature of interest is equal to the change ΔE_g in the bandgap energy E_g over the same temperature range. This moves the vacancy and divacancy ionization levels shown in Figure 19 and the conduction band energy E_c closer to the valence band energy E_v by an amount

ΔE_g. The antimony ionization level maintains a constant energy difference with respect to the conduction band (51). At a temperature T the values of the ionization levels with respect to the valence band energy $E_v = 0$ are given by:

$$E(V^-) = 0.42 - \Delta E_g(T)$$

$$E(V^{-2}) = 0.88 - \Delta E_g(T)$$

$$E(V_2^-) = 0.51 - \Delta E_g(T)$$

$$E(V_2^{-2}) = 0.77 - \Delta E_g(T)$$

$$E_c - E(Sb) = 0.04$$

The change $\Delta E_g(T)$(eV) in the bandgap energy is calculated from the empirical Varshni equation (52)

$$\Delta E_g(T) = E_g(T) - E_g(0) = (4.73 \times 10^{-4}T^2)/(T + 636) \quad \text{ev} \quad 4.18$$

The concentration of electrons in the conduction band [e^-] and holes in the valence band [h^+] as functions of E_F are needed to calculate the Fermi Level E_F. These are given by (53)

$$[e^-] = N_c \exp(-(E_c - E_F)/kT) \qquad 4.19$$

$$[h^+] = N_v \exp(-(E_F - E_v)/kT) \qquad 4.20$$

The effective density of states of the conduction band N_c and the effective density of states for the valence band N_v are given by (54)

$$N_c = 4.83 \times 10^{15}(Tm_c^*/m_0)^{1.5} \text{ cm}^{-3}$$

$$N_v = 4.83 \times 10^{15}(Tm_v^*/m_0)^{1.5} \text{ cm}^{-3}$$

In the above m_c^* and m_v^* are the density of states effective masses for the conduction and valence bands respectively and m_0 is the electron rest mass. The values used in this work are the highest temperature values (600°K) given by Barber (55):

$$m_c^*/m_0 = 1.28$$

$$m_v^*/m_0 = 0.92$$

Thurmond (52) presents data for $(m_c^* m_v^*/m_0^2)^{1/2}$ which suggests that the values of m_c^* and m_v^* for T > 600°K do not change by more than 10% from the 600°K values quoted above.

The Fermi Level E_F has the value which satisfies the condition of electrical neutrality (56):

$$[e^-] + [V^-] + 2[V^{-2}] + [V_2^-] + 2[V_2^{-2}] = [h^+] + [Sb^+] \qquad 4.21$$

In practice E_F can be obtained in a trial and error manner. An initial guess for

E_F is used to calculate each side of 4.21 using equations 4.11 - 4.15 and 4.19 - 4.20. If the left-hand side of equation 4.21 is greater than the right-hand side, the initial guess for E_F was too high and it should be reduced in the next iteration. If the converse is true, the value of E_F was too low and it should be raised in the next iteration. By using an initial guess of $E_F = E_g/2$ and then changing the guess by successively smaller values ($E_g/4$, $E_g/8$, $E_g/16$ . . .), this process converges rapidly to a value of E_F which satisfies equation 4.21 with the required accuracy. A listing of the author's program which implements these calculations is in Appendix D.

For this research, the primary interest is the effect of dopant concentration on the total effective vacancy concentration $[V_{TE}]$. The effect is shown by computing the ratio of $[V_{TE}]$ for heavily doped material to $[V_{TE}]$ for lightly doped ($N_D < 1 \times 10^{16}$ cm^{-3} *n*-type) material.

Figures 20 and 21 show this ratio as a function of temperature for *n*-type dopant concentrations of 5.0×10^{17} cm^{-3} (0.034 ohm-cm) and 1.0×10^{18} cm^{-3} (0.023 ohm-cm). It is apparent from these figures that heavily doped *n*-type silicon at temperatures below 900°K will have substantially higher equilibrium total effective vacancy concentrations than lightly doped material.

The total vacancy concentration ($[V^x] + [V^-] + [V^{-2}]$) exceeds the total divacancy concentration ($[V_2^x] + [V_2^-] + [V_2^{-2}]$) by at least one order of magnitude for temperatures below 1150°K and *n*-type dopant concentrations below 1×10^{18} cm^{-3}. In this range we can approximate equation 4.17 by:

$$[V_{TE}] = [V^x] + [V^-] + [V^{-2}] \qquad 4.22$$

The ionized vacancy concentrations are directly proportional to $[V^x]$ as shown by equations 4.11 and 4.12. Equation 4.22 can then be written:

$$[V^x] = [V_T]/M(E_F,T) \qquad 4.23$$

The proportionality factor M is a function of the fermi level E_F and the temperature T and $[V_T]$ is the total concentration of all vacancies in the silicon. Using equations 4.2 and 4.23 the chemical potential of neutral vacancies can be related to the total vacancy concentration:

$$\mu(V^x) = \mu^0(V^x) + KT \ln(([V_T]/M)/N_L)$$

$$= \mu^0(V^x) + KT \ln([V_T]/N_L^*) \qquad 4.24$$

where $N_L^* = MN_L$.

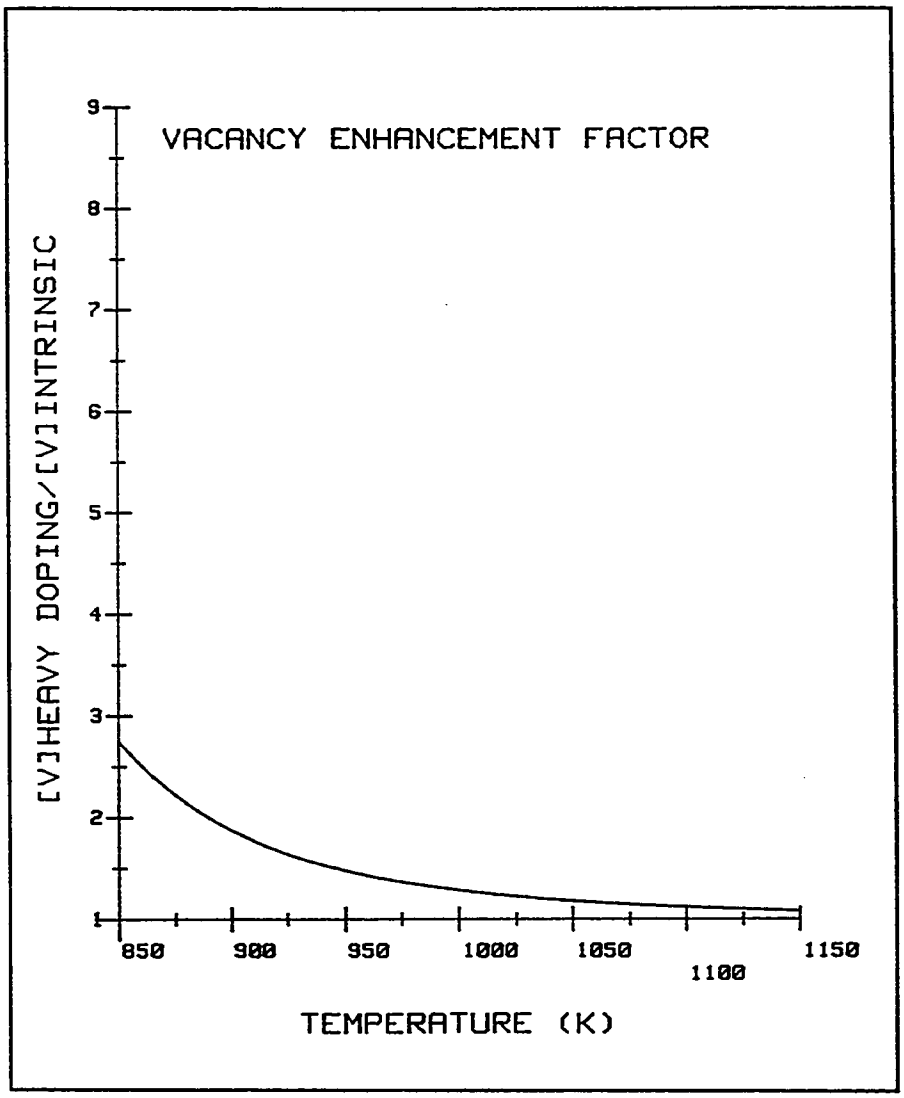

Figure 20. Total vacancy concentration for heavily doped material (N_D = 5 x 10^{17} cm^{-3}) as a function of temperature.

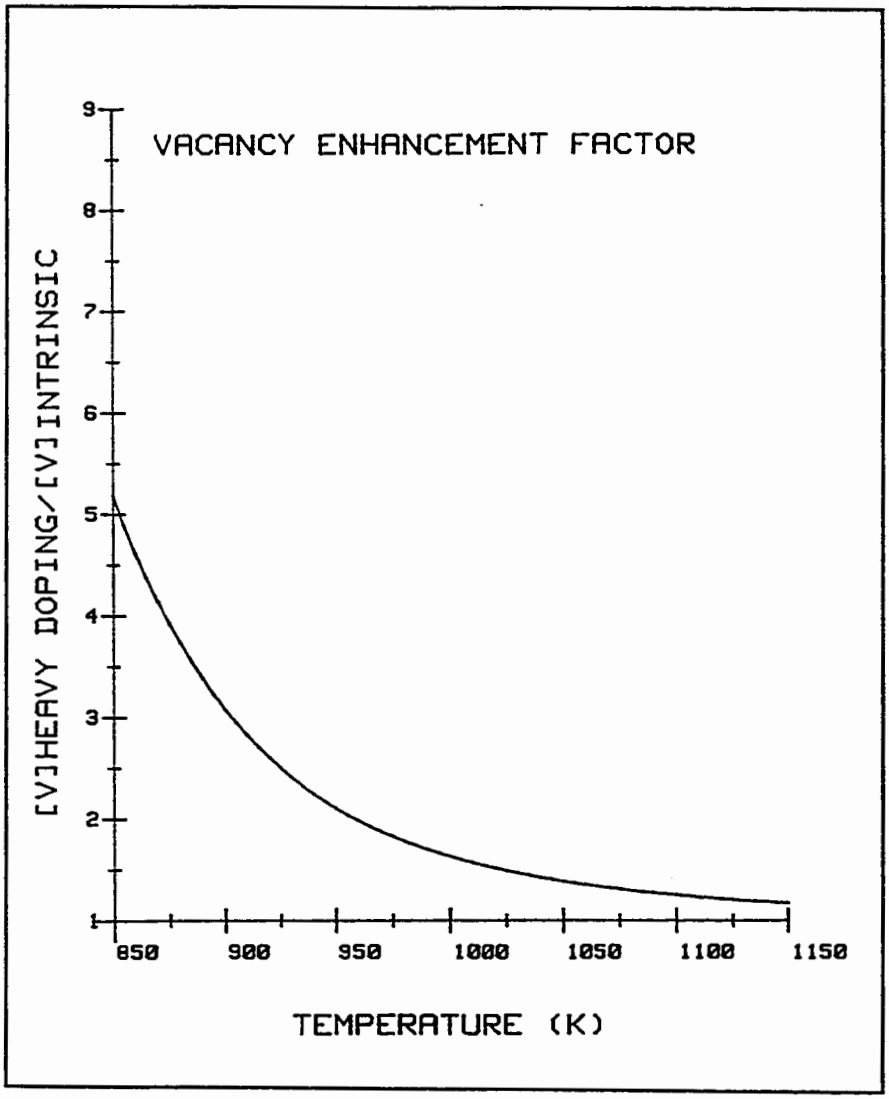

Figure 21. Total vacancy concentration for heavily doped material (N_D = 1 x 10^{18} cm^{-3}) as a function of temperature.

4.3 EFFECT OF VACANCY CONCENTRATION ON OXYGEN PRECIPITATE NUCLEATION

The reaction of an interstitial oxygen atom O_i with a silicon atom Si at a lattice site on the surface of an oxygen precipitate with an infinite radius can be represented as (57):

$$(1+X)Si + 2O_i + X_1V \rightharpoonup SiO_2 + X_2I$$

where $X_1 + X_2 = X \approx 1$.

The vacancy V and interstitial I accommodate the volume change which occurs when silicon dioxide is formed. The molar volume of SiO_2 is approximately twice the molar volume of crystalline silicon so either vacancies must be absorbed or silicon interstitials emitted from the growing precipitate if very high strains are to be avoided. If we consider only the effect of vacancies, the above equation becomes:

$$2Si + 2O_i + V \rightharpoonup SiO_2 \qquad 4.25$$

The free energy change dG accompanying the incorporation of a single interstitial oxygen atom into the precipitate is:

$$dG = 0.5\mu(SiO_2) - \mu(Si) - \mu(O_i) - 0.5\mu(V) \qquad 4.26$$

Using equation 4.2 this can be written as:

$$dG = -\mu^0(1) - KT \ln([O_i]/N_o) - 0.5\mu^0(V) - 0.5KT \ln([V]/N_L) \qquad 4.27$$

where

$$\mu^0(1) = \mu^0(Si) - \mu^0(O_i) - 0.5\mu^0(SiO_2)$$

and $\mu^0(V)$ is the Standard Chemical Potential of a vacancy.

In equilibrium dG = 0 and equation 4.27 gives the equilibrium solubility $[O_i]_{eq}$ of oxygen in silicon:

$$[O_i]_{eq} = N_o \exp(-\mu^0(1)/KT)(N_L/[V])^{1/2} \exp(-\mu^0(V)/2KT) \qquad 4.28$$

Equation 4.28 predicts that as the vacancy concentration decreases the equilibrium solubility of oxygen increases. If the vacancy concentration is at its thermal equilibrium value equation 4.28 becomes:

$$[O_i]_{eq} = N_o \exp(-\mu^0(1)/KT)$$

Mikkelsen (58) gives the values

$N_o = 9 \times 10^{22}$ cm^{-3} (New ASTM)

$= 3.5 \times 10^6$ ppma (Old ASTM)

$\mu^0(1) = 1.52$ev $= 21.9$ Kcal/mole

Equation 4.26 describes the free energy change occurring for the incorporation of an additional oxygen atom into a precipitate with infinite radius. The oxygen precipitation nucleation process actually involves particles with radii ≈ 10Å. In this case there is an additional contribution to the free energy change due to the energy required to increase the surface area of the precipitate. The free energy G of a precipitate of radius r containing N oxygen atoms is (59):

$$G(\text{precipitate}) = NdG + 4\pi r^2\sigma \qquad 4.29$$

where σ is the surface free energy per unit area. If v is the equivalent volume per oxygen atom in the precipitate then:

$$(4/3)\pi r^3 = Nv \qquad 4.30$$

Substituting 4.30 into 4.29 yields:

$$G(\text{precipitate}) = NdG + 4\pi\sigma N^{2/3}(3v/4\pi)^{2/3} \qquad 4.31$$

G(precipitate) exhibits a maximum at a value N(critical). For values of N < N(critical) the free energy of the precipitate increases as N increases while N > N(critical) the free energy of the precipitate decreases as N increases. Precipitates with N < N(critical) are thermodynamically unstable and will tend to dissolve. Precipitates with N > N(critical) are also thermodynamically unstable and will tend to grow. Only precipitates with N = N(critical) are in thermodynamic equilibrium. The value for N(critical) can be obtained by differentiating 4.31 with respect to N and setting the derivative equal to zero:

$$0 = dG + 4\pi\sigma(3v/4\pi)^{2/3}(2/3)N^{-1/3} \qquad 4.32$$

Using equation 4.30 and solving 4.32 for N yields the critical radius of the precipitate for N = N(critical):

$$r(\text{critical}) = -2\sigma v/dG \qquad 4.33$$

Substitution of 4.33 into equation 4.29 yields the free energy nucleation barrier G(r(critical)) that must be exceeded by thermal fluctuations in order to produce a precipitate capable of continued growth.

From equation 4.27 and 4.33 we can determine the effect of vacancy concentrations on the G(r(critical)). As [V] decreases the magnitude of dG will decrease which will increase G(r(critical)). The rate of oxygen precipitate nucleation J is given by (60):

$$J = Z \cdot w^* \cdot n^*$$

n^* = density of nuclei with r = r(critical) at thermal equilibrium
$= n_I \exp(-G(r(critical))/KT)$

Z = Zeldovich factor $\approx 10^{-3}$

w^* = oxygen impingement frequency onto the nuclei with r = r(critical)

n_I = nucleation site density (heterogeneous nucleation) or oxygen concentration (homogenous nucleation)

Since a decrease in the vacancy concentration increases G(r(critical)), it would decrease J. This will in turn increase the amount of interstitial oxygen which remains in solution following a high temperature cycle. The residual interstitial oxygen concentration C_R remaining after a high temperature thermal cycle is related to J by (60):

$$C_R = C_I - Jt_N V_p C_s$$

where

C_I = initial oxygen concentration

t_N = duration of the nucleation cycle

V_p = average volume of a precipitate

C_s = average number of oxygen atoms in the precipitate per cm^3.

The vacancy concentration can only affect the nucleation rate when it differs from

its thermal equilibrium value since the sum of the last two terms on the right hand side of equation 4.27 is zero in thermal equilibrium. Several authors present evidence that the point defect concentrations in silicon are not in equilibrium. Gosele (61) states:

> In most oxidation experiments a self-interstitial supersaturation ($S_I > 0$) is realized, but for high temperature and thick oxides, especially for (111) surface orientation as well as for oxidation in an ambient containing a chlorine compound a vacancy supersaturation ($S_I < 0$) may be generated.

The effects of point defect concentrations established during crystal growth on oxygen precipitate nucleation was studied by de Kock (62). Hahn et al (49) note that vacancies may be undersaturated in heavily Sb doped silicon due to the high equilibrium concentrations of charged vacancies in such material.

If the vacancy concentration is primarily determined by early high temperature processing then from equation 4.24 we would expect the chemical potential of vacancies in heavily doped material at low temperatures (< 1000°K) would be more negative than in lightly doped materials at the same temperature. At high temperatures (>1300°K) the total equilibrium vacancy concentration is nearly independent of the dopant concentration. For example, at a temperature of 1400°K $[V_T] = 1.2 \times 10^{17} cm^{-3}$, $[V^x] = 2.3 \times 10^{15}\ cm^{-3}$ and M = 51 in lightly doped ($N_D < 1 \times 10^{15}\ cm^{-3}$) silicon. At the same temperature with an antimony concentration of $1 \times 10^{18}\ cm^{-3}$, $[V_T] = 1.3 \times 10^{17}\ cm^{-3}$, $[V^x] = 2.3 \times 10^{15}\ cm^{-3}$ and M = 54. However, at 800°K in lightly doped silicon, $[V_T] = 5.2 \times 10^{10}\ cm^{-3}$, $[V^x] = 7.6 \times 10^{8}\ cm^{-3}$ and M = 66, but $[V_T] = 8.6 \times 10^{11}\ cm^{-3}$, $[V^x] = 7.6$

x 10^8 cm^{-3} and M = 1.1 x 10^3 in the heavily doped material. All these values assume the system is in thermal equilibrium. In the non-equilibrium case $[V_T]$ could be the same in both lightly and heavily doped materials having been established at a previous high temperature process. Then the vacancy chemical potential in the heavily doped material will be lower than the vacancy chemical potential in the lightly doped material by:

$$KT \ln(M(\text{lightly doped})/M(\text{heavily doped}))$$

$$KT \ln(66/1.1 \times 10^3) = -2.8\ KT$$

Equation 4.27 shows that this change in the chemical potential is equivalent to a four-fold reduction in the interstitial oxygen concentration. This equivalent reduction would explain the observed reduction in precipitation in heavily doped *n*-type material (47,48). This difference in chemical potential will occur regardless of the actual value of $[V_T]$ as long as $[V_T]$ has the same (non-equilibrium) value in both materials. A three-step thermal process is commonly used to achieve precipitation of oxygen in silicon (5,12). The first step occurs at a high temperature (T ≥ 1000°C) and is used to reduce by out-diffusion the oxygen concentration in the near surface region of the silicon wafer. The second step occurs at a lower temperature (T ≈ 700°C) and produces the precipitate nuclei which will grow in the third high temperature (T ≥ 900°C) step. Such three step processes produce a high density of precipitates in the center of the wafer and a precipitate-free region (denuded zone) at the surfaces of the wafer. A denuded zone is required for the proper operation of the semiconductor devices located on

the wafer surfaces (12). The high temperature out-diffusion step may determine the vacancy concentration of the silicon during the following nucleation step. This can occur if the rate of generation or reduction of vacancies is much slower at the nucleation temperature compared to the rate at the out-diffusion temperature (63). As discussed above, the vacancy chemical potential and the nucleation rate J in heavily doped material would then be lower than in lightly doped material. The following section presents data from an experimental study of nucleation in lightly and heavily doped material.

4.4 EXPERIMENTAL STUDY OF OXYGEN PRECIPITATION

The theory of Section 4.3 predicts that the dopant concentration can affect the nucleation rate of oxygen in silicon. The magnitude of this effect is dependent upon both the nucleation temperature and the dopant concentration with the largest effect occurring at the highest dopant concentrations and the lowest temperatures. To examine the effect of dopant concentration on nucleation a series of three-step precipitation cycles were performed on lightly and heavily doped material. The heavily doped silicon wafers originated from four different 100 mm diameter (100) orientation crystals with antimony dopant concentrations ranging from 3 to 5 X 10^{17} cm^{-3}. The relative location in the crystal from which each wafer originated was known for all of the heavily doped wafers. Figure 20 shows that such material will have equilibrium vacancy concentrations 1.2 to 3 times higher than lightly doped (intrinsic) material over the temperature range

550°C to 750°C. The lightly doped silicon wafers came from several 100 mm diameter (100) orientation crystals with boron dopant concentrations less than 4 x 10^{14} cm^{-3}. All wafers were polish etched in an 8:1 mixture of concentrated nitric acid and hydrofluoric acid to clean the wafers and to remove any surface damage. The techniques discussed in Chapters II and III were used to measure the interstitial oxygen concentrations in the wafers. The oxygen concentrations ranged from 21.7 ppma to 33.4 ppma for the heavily doped wafers and from 23.8 ppma to 29.2 ppma for the lightly doped wafers.

Groups of wafers from each ingot were annealed at 1100°C in a quartz tube diffusion furnace for one hour in an ambient of argon containing approximately 5% oxygen. The addition of a small percentage of oxygen to the argon prevents pitting of the wafer surface. This high temperature out-diffusion step dissolves any nuclei formed in the silicon during the crystal growth process (5) and helps establish a uniform point defect concentration in all wafers. The wafers were then cleaved into quarters and each quarter received one of the following nucleation cycles:

a. No Nucleation Cycle.

b. 550°C for 64 hours

c. 650°C for 64 hours

d. 750°C for 64 hours

The ambient for the above thermal cycles was argon with 5% oxygen. All quarters except for the quarter which received no nucleation anneal were then annealed at 1050°C for 16 hours in an ambient of argon with 5% oxygen. This 1050° C process allows the nuclei established in the previous step to grow as oxygen diffuses to and precipitates at the nuclei.

A second test was performed using 16 hours for the nucleation time instead of 64 hours. Several articles have reported that use of a pure oxygen ambient instead of an inert (argon or nitrogen) ambient can affect the point defect concentrations in the silicon (5,12,64). To investigate this effect a third test was performed using pure oxygen as the ambient during the out-diffusion and 64 hour nucleation steps. The results of the first test (argon ambient) are shown in Table VII.

TABLE VII

WAFER IDENTIFICATION, INITIAL OXYGEN, OXYGEN REMAINING AT END OF PROCESS FOR WAFERS WHICH RECEIVED NUCLEATION ANNEALS AT 550°C, 650°C, 750°C.

I.D.	INITIAL	550°C	650°C	750°C
1	23.79	22.35	17.20	18.58
2	22.55	20.73	19.63	20.38
3	21.74	20.35	9.82	7.89
4	23.99	21.75	18.79	14.47
5	22.73	22.35	17.82	18.43
6	26.57	25.56	15.12	21.04
7	22.79	23.28	18.05	20.80
8	24.02	20.94	18.84	19.38
9	22.88	24.17	18.84	20.66
10	30.51	29.47	10.07	18.96
11	32.90	31.82	10.07	21.57
12	33.40	28.17	11.69	26.19
13	33.40	28.46	11.45	24.21
14	27.75	26.14	11.55	21.35
15	27.41	26.10	12.86	20.59
16	29.21	27.01	11.12	25.56
17	27.78	26.35	11.17	21.96
18	27.63	26.35	12.28	21.96
19	27.98	26.10	11.25	24.73
20	26.18	25.51	13.49	24.55
21	29.18	26.83	11.42	25.47
22	23.78	24.40	15.35	23.23
23	29.87	28.79	10.30	9.31
24	25.44	23.78	12.90	9.30
25	28.11	27.90	10.32	7.50
26	28.39	27.23	10.60	7.38

The column labeled INITIAL gives the oxygen concentration of the wafers which received only the 1100°C 1-hour anneal. The columns labeled 550°C, 650°C and 750°C give the interstitial oxygen concentration (final oxygen) remaining in the

wafers after a 550°C, 650°C or 750°C nucleation anneal and the subsequent 16 hour 1050°C anneal. Wafers 1-5, 6-9, 10-14 and 23-26 are from the four heavily doped ingots. Wafers 15-22 are from the lightly doped ingots. An epitaxial layer was grown on wafers 23-26 and then chemically removed prior to the thermal cycles. The data in Table VII is presented graphically in Figures 22 to 26. Figures 22 to 24 plot Delta Oxygen (initial oxygen - final oxygen) versus initial oxygen for each of the nucleation temperatures. Figures 25 and 26 plot the fraction of the supersaturated oxygen which is precipitated versus the initial oxygen for the wafers which received the 650°C and 750°C anneals. This fraction is given by (initial oxygen-final oxygen)/(initial oxygen - 5.73 ppma). The term 5.73 ppma is the equilibrium oxygen solubility at 1050°C (1323°K) from equation 4.28.

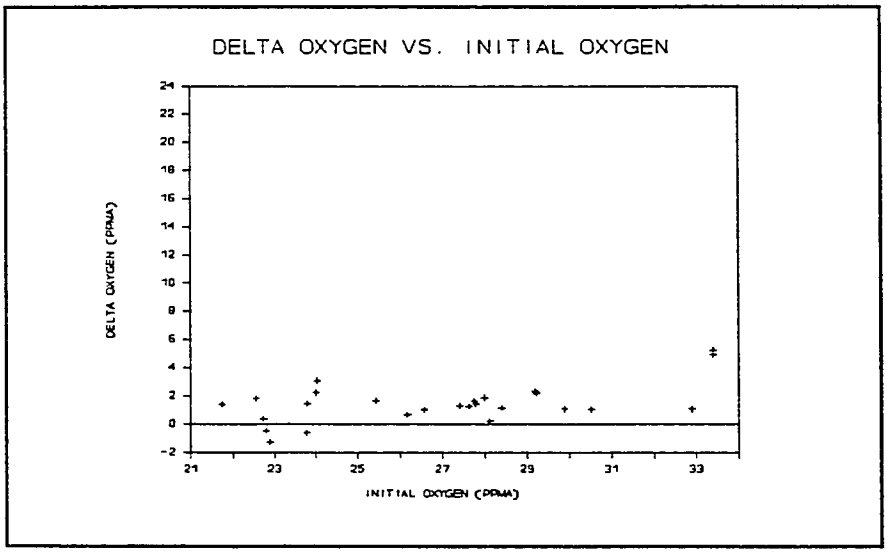

Figure 22. Plot of delta oxygen vs. initial oxygen for a nucleation temperature of 550°C.

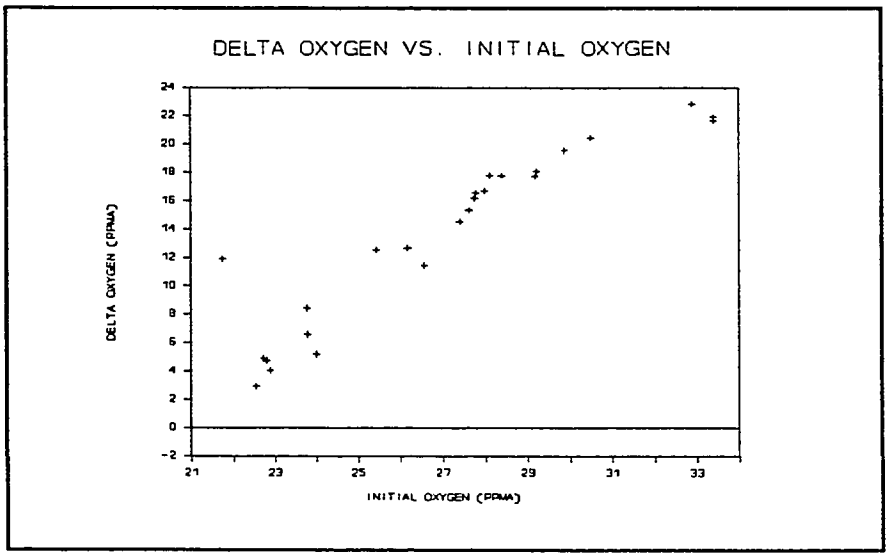

Figure 23. Plot of delta oxygen vs. initial oxygen for a nucleation temperature of 650°C.

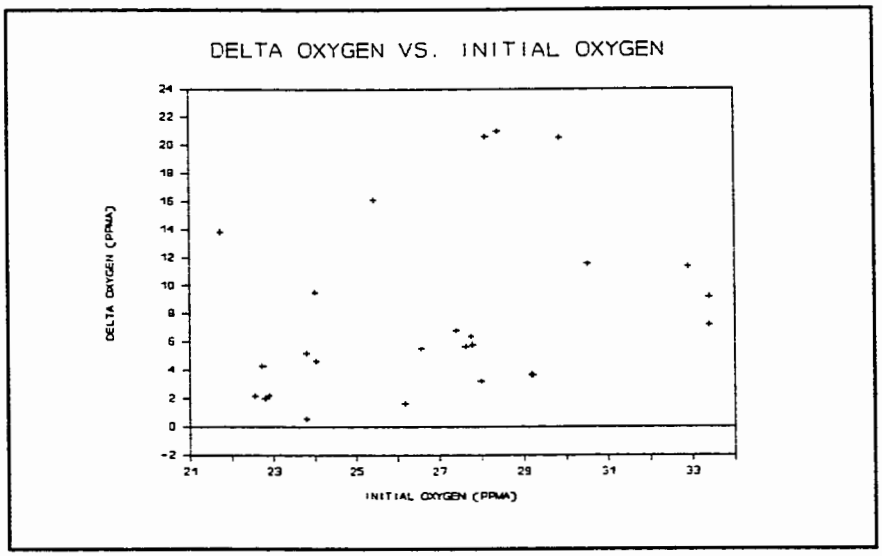

Figure 24. Plot of delta oxygen vs. initial oxygen for a nucleation temperature of 750°C.

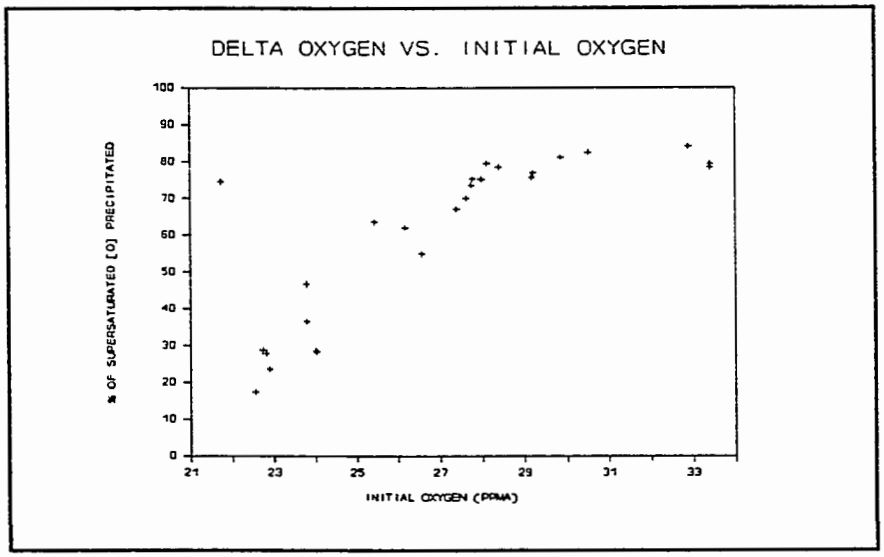

Figure 25. Plot of % supersaturated oxygen precipitated vs. initial oxygen for nucleation temperature of 650°C.

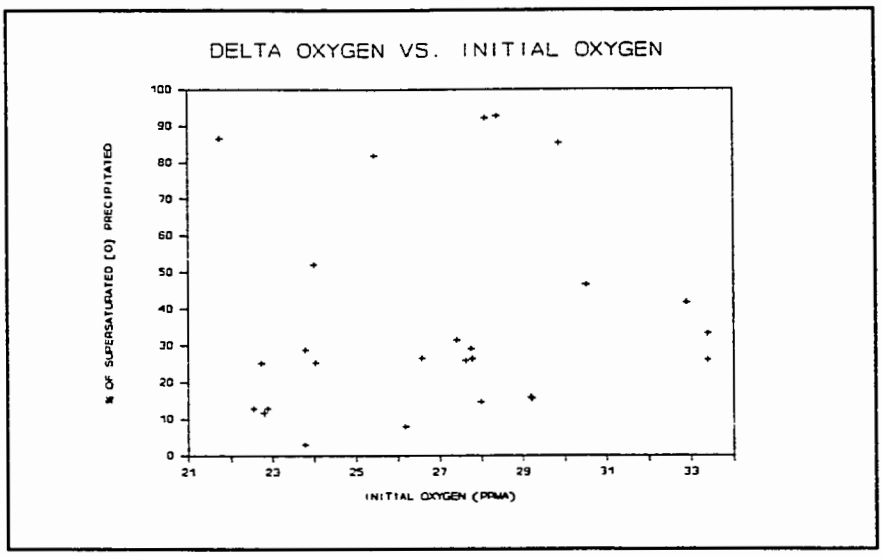

Figure 26. Plot of % supersaturated oxygen precipitated vs. initial oxygen for a nucleation temperature of 750°C.

Figure 22 shows that very little precipitation occurs after a 550°C nucleation cycle for initial oxygen concentrations less than 33 ppma. There is no apparent difference in behavior between heavily doped and lightly doped silicon.

Figures 23 and 25 show a regular behavior of the amount of oxygen precipitated with the initial oxygen concentration. It is apparent from Figure 25 that for initial oxygen concentrations greater than 29 ppma, the oxygen in wafers that received the 650°C preanneal is near equilibrium solubility. For oxygen concentrations less than 29 ppma the amount of oxygen precipitated is determined by the nucleation rate. As with Figure 22, there is no apparent difference in behavior between the lightly doped and heavily doped material. Only one point in the graphs of Figures 23 and 25 shows anomalous behavior. This point at

21.7 ppma corresponds to wafer 3 in Table VII. This wafer came from the tang end of the crystal. The tang end is the last part of the crystal to be solidified. Such behavior is consistent with the often observed anomalous precipitation behavior of material from the extreme ends of silicon crystals (5,65).

Figures 24 and 26 show the precipitation behavior of wafers which received the 750°C nucleation anneal. A comparison of Figures 25 and 26 shows that the 750°C anneal generally produces less precipitation with more variation in the amount precipitated for a given initial oxygen concentration. Five points in Figure 26 show precipitation close to the equilibrium solubility limit. One point corresponds to wafer #3 which came from the tang end of the crystal. The other four points correspond to wafers 23-26 in Table VII. These are the wafers which received the epitaxial layer prior to the thermal processing. Since wafer 23 came from the seed end of the crystal, wafer 24 came from the tang end and wafers 25 and 26 came from the center of the crystal, it appears that the anomalous precipitation behavior is attributable to the epitaxial processing and not to crystal position. It is interesting that the 650°C anneal did not show any anomalous effect due to the epitaxial processing. Excepting the epitaxial wafers, there is no apparent difference in precipitation behavior between the lightly doped and heavily doped materials for 750°C nucleation cycles.

As mentioned above, this test was repeated for a shorter nucleation time and for an oxygen instead of an argon ambient. These tests used heavily doped wafers which were adjacent in the crystal to the wafers used in the test discussed

above. This allowed for a direct comparison of the precipitation behavior of the wafers in the different tests. It was determined that the precipitation behavior of the wafers treated in the oxygen ambient was identical within measurement error to the behavior of the wafers treated in the argon ambient. In the test with the 16 hour nucleation cycle only the three wafers with initial oxygen concentrations greater than 30 ppma showed measurable precipitation. This indicates that nucleation times in excess of 16 hours are required to obtain precipitation when the initial oxygen concentration is below 30 ppma.

The wafers listed in Table VII were cleaved and Secco etched (66) for five minutes to delineate the bulk defects. Figures 27 to 29 show the etched cleavage face for wafer 14. The thickness of the wafers in Figures 27 to 29 is 475 microns. The cleavage faces shown in Figures 27 to 29 are generally typical of the appearance of the other wafers in Table VII. All cleavage faces for the 550°C nucleation anneal were virtually free of defects as would be expected given the small change in oxygen concentration that occurred during processing.

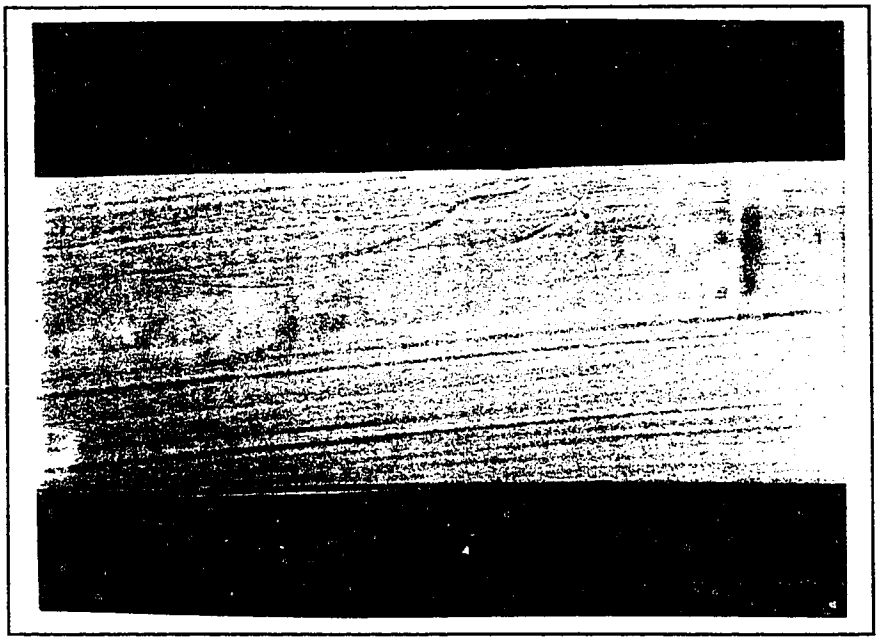

Figure 27. Secco etched cleavage face of wafer quarter processed using 550°C nucleation cycle.

Figure 28 shows the cleavage face of the wafer quarter processed using the 650°C anneal. The typical defects found in these cases are bulk stacking faults. The cleavage face in Figure 28 shows a rather uniform distribution of stacking faults throughout the interior of the wafer. The wafers which had initial oxygen concentrations below 23 ppma had a distribution of stacking faults which was low in the center of the wafer and increased towards the surface. This indicates that surface reactions control the nucleation/precipitation in materials with low oxygen concentrations.

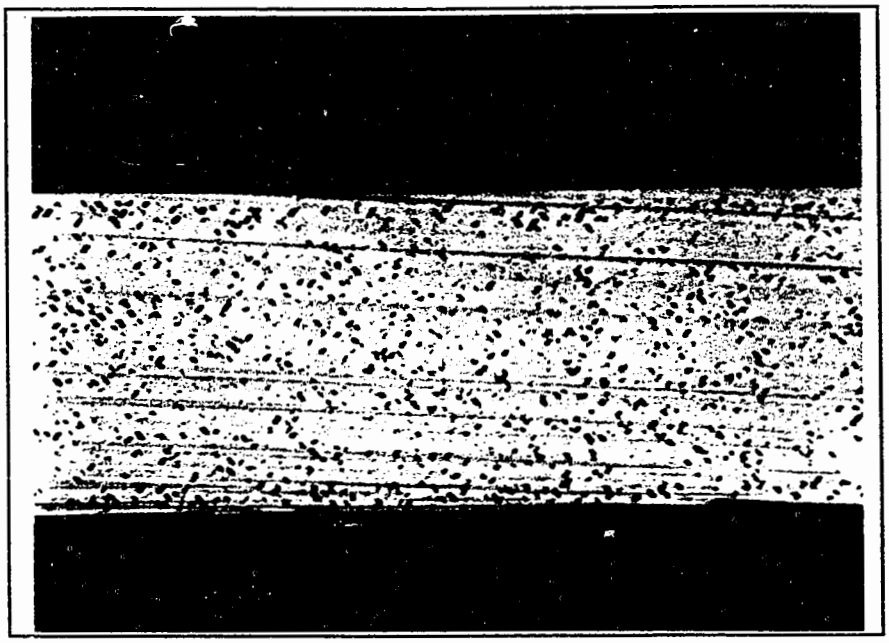

Figure 28. Secco etched cleavage face of wafer quarter processed using 650°C nucleation cycle.

In contrast, the cleavage faces of wafers processed using the 750°C anneal showed generally low densities of stacking faults. The predominant defect in these cleavage faces appeared to be etched out oxygen precipitates or small dislocation loops. Figure 29 shows the typical appearance of the cleavage face of a wafer processed with the 750°C anneal. The exception to this occurred for the wafers which had received the epitaxial processing. In these cases the cleavage faces for the 650°C and 750°C anneals appeared to be similar with the major defect being bulk stacking faults.

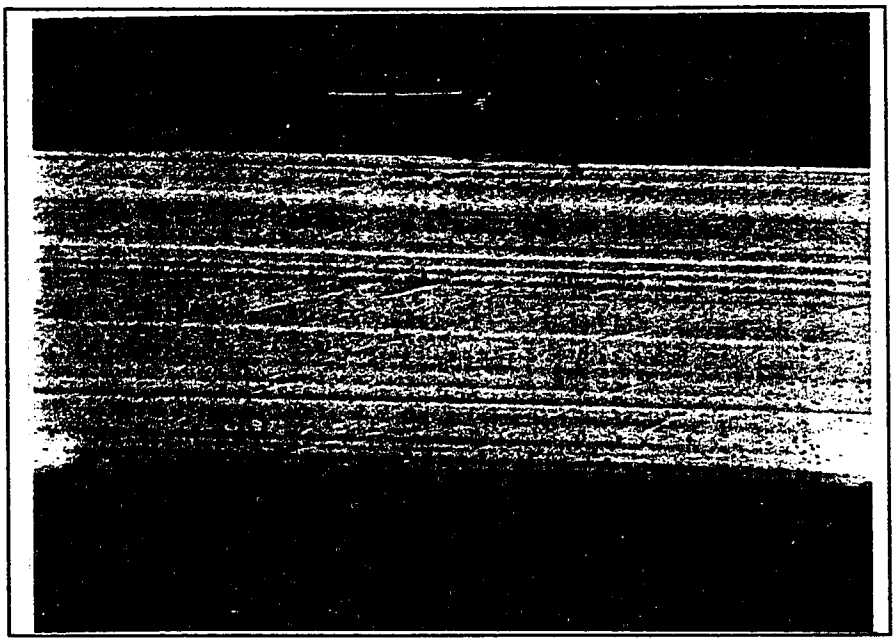

Figure 29. Secco etched cleavage face of wafer quarter processed using 750°C nucleation cycle.

In summary, the results of these experimental observations are:

1) The nucleation/precipitation reactions which occur in lightly doped *p*-type material during a three step anneal are indistinguishable from the reactions occurring in heavily antimony doped *n*-type material for $N_D \leq 5 \times 10^{17}$ cm^{-3}.

2) The 650°C and 750°C nucleation anneals produce different bulk defects. This is in agreement with previous TEM work which identified different bulk defects associated with different annealing temperatures (67,68).

3) A change in ambient from inert (argon) to oxidizing (dry oxygen) during the nucleation cycle does not affect the observed nucleation/ precipitation.

4) The epitaxial process affects the degree of oxygen precipitation and the type of bulk defects produced for wafers processed using the 750°C nucleation anneal.

The result 1) above is contrary to the behavior expected using the theory presented in Section 4.3. There are two explanations for this discrepancy:

a) Equilibrium concentrations of vacancies are rapidly established so that the change in free energy dG from equation 4.27 is independent of the vacancy concentration. This explanation is not likely due to the spatial variations observed in the precipitation of low oxygen material.

b) The increase in the equilibrium total vacancy concentration is smaller than predicted using the methods of Section 4.2. This discrepancy may be due to the uncertainty in the value of the effective masses. If the effective masses are larger than the values assumed in Section 4.2, the Fermi level will be closer to the middle of the band gap and the total vacancy concentration for the heavily doped material will be lower than predicted in Figure 20. In this case we would need to use material with a larger dopant concentration in order to observe the effect of vacancy concentrations on nucleation. This is the likely explanation for the similarity in behavior between the lightly and heavily doped material used in this study.

CHAPTER V

CONCLUSION

It has been shown that the accurate measurement of oxygen in silicon can be extended, using the techniques described above, to silicon with optically rough surfaces, silicon with a large amount of precipitated oxygen, and heavily doped *n*-type silicon. A relationship was developed which determines the limit of accurate oxygen measurement for heavily doped silicon as a function of the performance of the spectrometer and the properties of the sample. This relationship yielded an optimal absorbance which differs from the optimal absorbance used in spectrophotometry.

Optimization of the S/N of the FTIR spectrometer using the methods described in Chapter III in conjunction with heavily doped samples of the optimal thickness enables infrared interstitial oxygen measurements previously considered infeasible. This extension of the oxygen measurement technique is expected to be widely used in the future for quality and process control and for research into the properties of point defects in silicon.

Chapter IV presented a model which explains the observed reduction of nucleation/precipitation in heavily doped *n*-type material. A series of nucleation/precipitation experiments conducted on silicon with an antimony

dopant concentration of 5 x 10^{17} cm^{-3} showed that there were no apparent differences in the interstitial oxygen changes compared with lightly doped material. This is in agreement with previously published results (40) which found that *n*-type dopant concentrations in excess of 1 x 10^{18} cm^{-3} suppressed the appearance of bulk defects. The results from Chapter IV also showed that heavily doped slices which received an epitaxial layer had greater precipitation after a thermal cycle with a 750°C nucleation anneal than similarly processed lightly doped wafers. In general, the experiments showed that 650°C nucleation cycles produced a more consistent precipitation behavior than 750°C nucleation cycles.

LIST OF REFERENCES

1. E. Sirtl, *Semiconductor Silicon 1981*, H.R. Huff, R.J. Kriegler and Y. Takeishi, Eds. (The Electrochemical Society, Pennington, N.J., 1981), p. 157.

2. L.J. Cheng and D.C. Leung, *Electronic and Optical Properties of Polycrystalline or Impure Semiconductors and Novel Silicon Growth Methods*, K.V. Ravi and B. O'Mara, Eds. (The Electrochemical Society, Pennington, N.J., 1980) p. 157.

3. A.M. Salama, *Electronic and Optical Properties of Polycrystalline or Impure Semiconductors and Novel Silicon Growth Methods*, K.V. Ravi and B. O'Mara, Eds. (The Electrochemical Society, Pennington, N.J., 1980) p. 114.

4. W.K. Tice and T.Y. Tan, *Defects in Semiconductors*, J. Narayan and T.Y. Tan, Eds. (North-Holland, N.Y., 1981), p. 367.

5. J.H. Matlock, *Silicon Processing*, D.C. Gupta, Ed. (American Society for Testing and Materials, Philadelphia, Pa., 1983), p. 332.

6. ASTM F121-83, *Book of SEMI Standards 1988*, (Semiconductor Equipment and Materials International, Mountain View, Ca, 1988).

7. R.J. Bleiler, R.S. Hockett, P. Chu, and E. Strathman, *Oxygen, Carbon, Hydrogen and Nitrogen in Crystalline Silicon*, J.C. Mikkelsen, S.J. Pearton, J.W. Corbett, S.J. Pennycook, Eds. (Materials Research Society, Pittsburgh, Pa., 1986), p. 73.

8. H. Walitzki, H.J, Rath, J. Reffle, S. Pahlke, and M. Blatte, *Semiconductor 1986*, H.R. Huff, T. Abe and B. Kolbesen, Eds. (The Electrochemical Society, Pennington, N.J., 1986), p. 86.

9. J.A. Van Vechten, *Handbook on Semiconductors* Vol. 3, S.P. Keller, Ed. (North-Holland, Amsterdam, 1980), p. 80.

10. A. Baghdadi, *Semiconductor Processing*, D.C. Gupta, Ed. (American Society for Testing and Materials, Philadelphia, Pa., 1984), p. 343.

11. T. Abe, S. Gotoh, N. Ozawa and T. Masui, *Silicon Processing*, D.C. Gupta, Ed. (American Society for Testing and Materials, Philadelphia, Pa., 1983), p., 469.

12. R.A. Craven, *Semiconductor Silicon 1981*, H.R. Huff, R.J. Kriegler, Y. Takeishi, Eds. (The Electrochemical Society, Pennington, N.J., 1981), p. 254.

13. J.G. Wilkes, Journal of Crystal Growth **65**, 214 (1983).

14. R.K. Graupner, *Silicon Processing*, D.C. Gupta, Ed. (American Society for Testing and Materials, Philadelphia, Pa., 1983), p. 459.

15. B. Pajot, Analusis **5**, No. 7, 293 (1977).

16. P. Stallhofer and D. Huber, Solid State Technology **26**, No. 8, 233 (1983).

17. ASTM F120-87, *Book of SEMI Standards 1988*, (Semiconductor Equipment and Materials International, Mountain View, Ca., 1988).

18. W. J. Patrick, *Silicon Device Processing*, C.P. Marsden, Ed. (National Bureau of Standards Special Publication 337, 1970) p. 442.

19. K. Graff, Journal of the Electrochemical Society **130**, 1379 (1983).

20. W.M. Bullis and W.C. O'Mara, *Defects in Silicon*, W. M. Bullis and L.C. Kimmerling Eds. (The Electrochemical Society, Pennington, N.J., 1983), p. 275.

21. S.P. Weeks, *Semiconductor Processing*, D.C. Gupta, Ed (American Society for Testing and Materials, Philadelphia, Pa., 1984), p. 335.

22. J.H. Moore, C.C. Davis and M.A. Coplan, *Building Scientific Apparatus* (Addison-Wesley, Reading, Ma., 1983), p. 433.

23. H.H. Willard, L.L. Merritt, J.A. Dean, *Instrumental Methods of Analysis*, (Van Nostrand, N.Y., 1974), p. 93.

24. C. Foskett and T. Hirschfeld, Applied Spectroscopy **31**, 239 (1977).

25. R.O. Carter, Applied Spectroscopy **40**, 272 (1986).

26. H. Mark and J. Workman, Spectroscopy **2**, No. 11, 38 (1987).

27. P.R. Griffiths and J.A. deHaseth, *Fourier Transform Infrared Spectrometry*, (John Wiley, N.Y., 1986), p. 98.

28. W.K. Gladden, "Study of Free Carrier Absorption in Silicon Using Fourier Transform Infrared Spectroscopy," M.S. thesis, University of Maryland, Baltimore Md., 1986.

29. W.K. Gladden and A. Baghdadi, *Emerging Semiconductor Technology*, D.C. Gupta and P.H. Langer, Eds. (American Society for Testing and Materials, Philadelphia, Pa., 1983), p. 353.

30. ASTM F723-82, *Book of SEMI Standards 1988*, (Semiconductor Equipment and Materials International, Mountain View, Ca, 1988).

31. A.W. Steele and G.M. Hieftje, Applied Spectroscopy **40**, 1117 (1986).

32. A. V. Oppenheim and R. W. Schafer, *Digital Signal Processing*, (Prentice-Hall, Englewood Cliffs, N.J., 1975), p. 125.

33. C. T. Foskett, Applied Spectroscopy **30**, 531 (1976)

34. P.R. Griffiths and J.A. deHaseth, *Fourier Transform Infrared Spectrometry*, (John Wiley, N.Y., 1986), p. 24.

35. B. Senitzky and S.P. Weeks, Journal of Applied Physics **52**, 5308 (1981).

36. U. Gosele, W. Frank, and A. Seeger, Applied Physics **23**, 361 (1980).

37. T.Y. Tan and B.J. Ginsberg, *Defects in Semiconductors II*, S. Mahajan and J.W. Corbett, Eds. (North-Holland, Amsterdam, 1983), p. 141.

38. A. S. Oates and R.C. Newman, Applied Physics Letters **49**, 262 (1986).

39. C.P. Ho and J.D. Plummer, Journal of the Electrochemical Society **126**, 1516 (1979).

40. A.J.R. de Kock and W.M. van de Wijgert, Journal of Crystal Growth **49**, 718 (1981).

41. U. Gosele and T.Y. Tan, *Defects in Semiconductors II*, S. Mahajan and J.W. Corbett, Eds. (North-Holland, Amsterdam, 1983), p. 45.

42. B.P.R. Marioton, U. Gosele, and T.Y. Tan, Chemtronics **1**, 156 (1986).

43. G.D. Watkins, *Deep Centers in Semiconductors*, S.T. Pantelides, Ed. (Gordon and Breach, N.Y., 1986), p. 147.

44. S. Dannefaer, P. Mascher and D. Kerr, Physical Review Letters **56**, 2195 (1986).

45. B. Tuck, *Introduction to Diffusion in Semiconductors*, (Peter Peregrinus, Stevenage, England, 1974), p. 97.

46. R.K. Jain and R.J. Van Overstraeten, IEEE Transactions on Electron Devices **21**, 155 (1974).

47. C.W. Pearce, T. Kook and R.J. Jaccodine, *Impurity Diffusion and Gettering in Silicon*, R.B. Fair, C.W. Pearce and J. Washburn, Eds. (Materials Research Society, Pittsburgh, 1985), p. 231.

48. W. Dyson and J. Makovsky, *Oxygen, Carbon, Hydrogen and Nitrogen in Crystalline Silicon*, J.C. Mikkelsen, S.J. Pearton, J.W. Corbett, S.J. Pennycook, Eds. (Materials Research Society, Pittsburgh, Pa., 1986), p. 293.

49. S. Hahn, M. Arst, Z.U. Rek, V. Stojanoff, D.A. Bulla, W.E. Castro, W.A. Tiller, Applied Physics Letters **50**, 401 (1987).

50. C. Kittel and H. Kroemer, *Thermal Physics*, (W. H. Freeman, N.Y., 1980), p. 267.

51. J.A. Van Vechten, *Microscopic Identification of Electronic Defects in Semiconductors*, N.M. Johnson, S.G. Bishop, G.D. Watkins, Eds. (Materials Research Society, Pittsburgh, Pa., 1985), p. 83.

52. C.D. Thurmond, Journal of the Electrochemical Society **122**, 1133 (1975).

53. C. Kittel and H. Kroemer, *Thermal Physics*, (W.H. Freeman, N.Y., 1980), p. 361.

54. J.S. Blakemore, *Solid State Physics* 2nd ed., (Cambridge Press, Cambridge, 1985), p. 301.

55. H.D. Barber, Solid-State Electronics **10**, 1039 (1967).

56. C. Kittel and H. Kroemer, *Thermal Physics*, (W.H. Freeman, N.Y., 1980), p. 357.

57. T.Y. Tan, *Oxygen, Carbon, Hydrogen and Nitrogen in Crystalline Silicon*, J.C. Mikkelsen, S.J. Pearton, J.W. Corbett, S.J. Pennycook, Eds. (Materials Research Society, Pittsburgh, Pa., 1986), p. 269.

58. J.C. Mikkelsen, *Oxygen, Carbon, Hydrogen and Nitrogen in Crystalline Silicon*, J.C. Mikkelsen, S.J. Pearton, J.W. Corbett, S.J. Pennycook, Eds. (Materials Research Society, Pittsburgh, Pa., 1986), p. 19.

59. C. Kittel and H. Kroemer, *Thermal Physics*, (W. H. Freeman, N.Y., 1980), p. 294.

60. N. Inoue, K. Wada and J. Osaka, *Semiconductor Silicon 1981*, H. R. Huff, R. J. Kriegler, Y. Takeishi Eds. (The Electrochemical Society, Pennington, N.J., 1981), p. 282.

61. U. Gosele, *Aggregation Phenomena of Point Defects in Silicon*, E. Sirtl, J. Goorissen Eds. (The Electrochemical Society, Pennington, N.J., 1983), p. 17.

62. A.J.R. de Kock, *Aggregation Phenomena of Point Defects in Silicon*, E. Sirtl, J. Goorissen Eds. (The Electrochemical Society, Pennington, N.J., 1983), p. 58.

63. D.A. Antoniadis and I. Moskowitz, *Aggregation Phenomena of Point Defects in Silicon*, E. Sirtl, J. Goorissen, Eds. (The Electrochemical Society, Pennington, N.J., 1983), p. 1.

64. S.M. Hu, Applied Physics Letter **36**, 561 (1980).

65. L. Jastrzebski, *Silicon Processing*, D.C. Gupta, Ed. (American Society for Testing and Materials, Philadelphia, Pa., 1983), p. 309.

66. F. Secco D'Aragona, Journal of the Electrochemical Society **119**, 948 (1972).

67. W.A. Tiller, S. Hahn and F.A. Ponce, Journal of Applied Physics **59**, 3255 (1986).

68. K. Temperhoff, B. Hahn and R. Gleichmann, *Semiconductor Silicon 1981*, H.R. Huff, R.J. Kriegler, Y. Takeishi, Eds. (The Electrochemical Society, Pennington, N.J, 1981), p. 244.

APPENDIX A

MRC PROGRAM TO CORRECT SPECTRA FOR EFFECT OF MULTIPLE REFLECTIONS

```
1.
2.    C                    PROGRAM MRC.ASC
3.    C                  BOB GRAUPNER  9/24/86
4.          INTEGER IHEAD(352), FSZS, OFN, FLOC,IDATA(352)
5.    C
6.    C DETERMINE FTIR PARAMETERS
7.    C
8.    C READ FILE SIZE IN SECTORS FROM LOCATION 6145
9.          FSZS=IRVAL(6145,1)
10.   C READ ORIGIN FILE NUMBER
11.         OFN=IRVAL(6163,1)
12.   C CALCULATE SECTOR LOCATION OF FILE STATUS BLOCK
13.         FLOC=(8320 + (OFN+1)*FSZS)-1
14.   C READ FILE STATUS BLOCK INTO IHEAD
15.         CALL IRDISK(IHEAD,352,FLOC)
16.         FLOC=(8320 + OFN*FSZS)
17.   C IHEAD(6)=VALUE OF EXPONENT
18.   C CALCULATE CHANGE IN WAVENUMBERS PER DATA POINT
19.   C IHEAD(17)=SSP
20.   C IHEAD(15)=NTP/256
21.         DELTA=(15798.2/IHEAD(17))/(128*IHEAD(15))
22.   C DETERMINE SECTORS FOR RANGE 600-2000
23.         ISEC1=INT(600.0/(DELTA*352))
24.         ISEC2=INT(2000.0/(DELTA*352))
25.   C
26.   C CALCULATE AND STORE SPECTRUM
27.   C
28.         WRITE(2,100)
29.   100   FORMAT(' PERFORM MRC ON %T SPECTRUM IN ORIGIN FILE>')
30.         WRITE(2,300)
31.   300   FORMAT(' OVER RANGE OF 600-2000 WAVENUMBERS')
32.         DO 500 ISEC=ISEC1,ISEC2
33.         CALL IRDISK(IDATA,352,FLOC+ISEC)
34.         DO 400 J=1,352
35.         WAVENUM=(ISEC*352+J-1)*DELTA
36.   C NO CHANGE IF DATA IS OUTSIDE OF RANGE
37.         IF(WAVENUM.LT.600.0) GOTO 400
38.         IF (WAVENUM.GT.2000.0) GOTO 400
39.   C EXPRESS T AS A REAL NUMBER 0.0< T < 1.0
40.         T=IDATA(J)*(2.0**(IHEAD(6)-19))
41.         CORFAC=0.5+0.5*SQRT(1.0+1.50*T*T)
42.         T=T/CORFAC
43.         IDATA(J)=T*(2.0**(19-IHEAD(6)))
44.   400   CONTINUE
45.         CALL IWDISK(IDATA,352,FLOC+ISEC)
46.   500   CONTINUE
47.         CALL IREXIT
```

APPENDIX B

PROGRAM AND MACRO FOR CALCULATIONS OF SPECTROMETER NOISE

```
#RESERVE 1000-43777
#LINK IRVAL
C PROGRAM TO CALCULATE THE STANDARD DEVIATION OF NOISE
C BETWEEN XSP AND XEP, NORMALIZING BY VALUE AT VI2
C ASSUMES DIFFERENCE SPECTRUM IS IN SAMPLE FILE
C ASSUMES SINGLE BEAM SPECTRUM IS IN REFERENCE FILE
C PROGRAM LISTS DATA POINTS IF VI3 .NE. 0
      INTEGER IHEAD(352),FSZ,SFN,RFN,IDATA(352),FLOC
C READ FILE SIZE IN SECTORS FROM LOCATION 6145
      FSZ=IRVAL(6145,1)
C READ SAMPLE FILE NUMBER
      SFN=IRVAL(6157,1)
C CALCULATE SECTOR LOCATION OF FILE STATUS BLOCK
      FLOC=8320+(SFN+1)*FSZ-1
C READ FILE STATUS BLOCK INTO IHEAD
      CALL IRDISK(IHEAD,352,FLOC)
C SET FLOC TO START OF SAMPLE FILE
      FLOC=(8320+SFN*FSZ)
C CHECK TRANSMITTANCE FLAG IN FILE STATUS BLOCK
      IF (IHEAD(9).EQ.0) THEN
          SCL=100.0
        ELSE
          SCL=1.0
      ENDIF
C CALCULATE SPACING BETWEEN DATA POINTS
      SSP=IHEAD(17)
      NTP=256*IHEAD(15)
      DELTA=((15798.2/SSP)/(0.5*NTP))
C WAVENUMBER RANGE FOR NOISE CALCULATION IS XSP TO XEP
      XEP=IRVAL(6165,1)
      XSP=IRVAL(6166,1)
C NOTE DEFINITION OF XEP AND XSP DIFFERS FROM NORMAL USAGE
      SUM=0.0
      ICUR=-1
      IEXP=IHEAD(6)
C LOAD FLAG TO TURN DATA LISTING OFF
      IVI3=IRVAL(6133,1)
C CALCULATE DATA POINT RANGE
      ISRT=INT((XSP/DELTA)+0.5)+1.0
      IXEP=INT((XEP/DELTA)+0.5)+1.0
C CALCULATE EXPONENT TO OBTAIN FLOATING POINT DATA
      EXP=(2.0**(19-IEXP))
C SUM SQUARE OF DIFFERENCES
      DO 4000 J=ISRT,IXEP-1,1
C CALCULATE SECTOR OF REQUESTED POINT
      ISEC=INT((J-.1)/352)
C CALCULATE LOCATION WITHIN SECTOR
```

```
      LOC=J-(352*ISEC)
C CHECK IF REQUESTED SECTOR IS IN MEMORY, LOAD IF NOT
      IF (ISEC.EQ.ICUR) THEN
          GOTO 2000
        ELSE
          CALL IRDISK(IDATA,352,FLOC+ISEC)
          ICUR=ISEC
      ENDIF
2000  X1=SCL*IDATA(LOC)/EXP
C CALCULATE SECTOR OF REQUESTED POINT
      ISEC=INT((J+1-.1)/352)
C CALCULATE LOCATION WITHIN SECTOR
      LOC=J+1-(352*ISEC)
C CHECK IF REQUESTED SECTOR IS IN MEMORY, LOAD IF NOT
      IF (ISEC.EQ.ICUR) THEN
          GOTO 3000
        ELSE
          CALL IRDISK(IDATA,352,FLOC+ISEC)
          ICUR=ISEC
      ENDIF
3000  X2=SCL*IDATA(LOC)/EXP
      WNUM=(J-1)*DELTA
      IF (IVI3.EQ.0) GOTO 3500
      PRINT 8000,WNUM,X1
3500  SUM=SUM+(X1-X2)**2
4000  CONTINUE
C PRINT LAST DATA POINT
      IF (IVI3.EQ.0) GOTO 4500
      WNUM=(IXEP-1)*DELTA
      PRINT 8000,WNUM,X2
C CALCULATE STANDARD DEVIATION
4500  SIGMA=SQRT(SUM/(2*(IXEP-ISRT)))
      PRINT *,' '
      PRINT 8050,SIGMA
C NORMALIZE S.D. TO VALUE AT VI2
C READ REFERENCE FILE NUMBER
      RFN=IRVAL(6168,1)
C CALCULATE SECTOR LOCATION OF FILE STATUS BLOCK
      FLOC=8320+(RFN+1)*FSZ-1
C READ FILE STATUS BLOCK INTO IHEAD
      CALL IRDISK(IHEAD,352,FLOC)
C SET FLOC TO START OF REFERENCE FILE
      FLOC=(8320+RFN*FSZ)
C LOAD VI2
      VI2=IRVAL(6132,1)
      IEXP=IHEAD(6)
C CALCULATE EXPONENT TO OBTAIN FLOATING POINT DATA
      EXP=(2.0**(19-IEXP))
C CALCULATE DATA POINT NUMBER
      ISRT=INT((VI2/DELTA)+0.5)+1.0
C CALCULATE SECTOR OF REQUESTED POINT
```

```
      ISEC=INT((ISRT-.1)/352)
C CALCULATE LOCATION WITHIN SECTOR
      LOC=ISRT-(352*ISEC)
      CALL IRDISK(IDATA,352,FLOC+ISEC)
      FXF=SCL*IDATA(LOC)/EXP
      WNUM=ISRT*DELTA
      PRINT *,'NORMALIZE BY:'
      PRINT 8000,WNUM,FXF
      PRINT *,' '
      SIGMA=100.0*SIGMA/FXF
      PRINT 8100,SIGMA
8000  FORMAT(' WAVENUMBER=',F9.2,'    VALUE=',E12.4)
8050  FORMAT(' STANDARD DEVIATION=',E12.4)
8100  FORMAT(' NORMALIZED STANDARD DEVIATION=',E12.4,'%')
      CALL IREXIT
      END
```

```
LST NOI


CLS
CLR
FPS
FPR
FCS=1
FCR=1
VI2=1105
PRN NSS
DIF
FCS=0.7071
MUS
XSP=1206
XEP=1006
GFN
NOISE2.000
FRN
END
```

```
NSS =       1

STANDARD DEVIATION=   .7244E-05
NORMALIZE BY:
WAVENUMBER=  1106.95    VALUE=   .1861E-01

NORMALIZED STANDARD DEVIATION=   .3892E-01%
```

APPENDIX C

PROGRAM NPLUS.ASC TO CALCULATE THE SYNTHETIC FREE CARRIER ABSORPTION SPECTRUM

```
1.
2.    C                    PROGRAM NPLUS.ASC
3.    C                  BOB GRAUPNER  9/11/86
4.    C                    REVISED 4/12/88
5.    C CALCULATES FREE CARRIER ABSORPTION AND STORES AN ABSORBANCE
6.    C SPECTRUM IN THE ORIGIN FILE. REQUIRES THAT THE ORIGIN FILE
7.    C BE A VALID ABSORBANCE FILE. ASSUMES N-TYPE DOPANT. SAMPLE
8.    C THICKNESS AND RESISTIVITY ARE INPUT FROM THE TERMINAL
9.          INTEGER IHEAD(352). FSZS. OFN. FLOC.IDATA(352)
10.   C
11.   C ENTER THICKNESS OF SAMPLE
12.   C
13.         WRITE(2,10)
14.   10    FORMAT(' ENTER SAMPLE THICKNESS IN CM   ')
15.         READ(1,20) D
16.   20    FORMAT(F10.4)
17.   C
18.   C ENTER SAMPLE RESISTIVITY
19.   C
20.         WRITE(2,100)
21.   100   FORMAT(' ENTER N-TYPE RESISTIVITY IN OHM-CM   ')
22.         READ(1,200) RES
23.   200   FORMAT(F12.6)
24.         WRITE(2,250)
25.   250   FORMAT(' ENTER FRACTION IONIZED')
26.         READ(1,275) PION
27.   275   FORMAT(F12.6)
28.   C
29.   C     CALCULATE CARRIER CONCENTRATION
30.   C
31.         A0=-3.1083
32.         A1=-3.2626
33.         A2=-1.2196
34.         A3=-0.13923
35.         B1=1.0265
36.         B2=0.38755
37.         B3=0.041833
38.         X=ALOG10(RES)
39.         ZU=A0+(A1*X)+(A2*X*X)+(A3*X*X*X)
40.         ZL=1.0+B1*X+(B2*X*X)+(B3*X*X*X)
41.         Z=ZU/ZL
42.         RN=(6.242E18/RES)*(10**Z)
43.         WRITE(2,300) RES,RN
44.   300   FORMAT(' N-TYPE RESISTIVITY=',F9.4,'OHM-CM    ',E12.2,
44.        0'ATOMS/CM3')
46.         RN=PION*RN
47.   C
```

```
C DETERMINE FTIR PARAMETERS
C
C READ FILE SIZE IN SECTORS FROM LOCATION 6145
      FSZS=IRVAL(6145,1)
C READ ORIGIN FILE NUMBER
      OFN=IRVAL(6163,1)
C CALCULATE SECTOR LOCATION OF FILE STATUS BLOCK
      FLOC=(8320 + (OFN+1)*FSZS)-1
C READ FILE STATUS BLOCK INTO IHEAD
      CALL IRDISK(IHEAD,352,FLOC)
      FLOC=(8320 + OFN*FSZS)
C IHEAD(6)=VALUE OF EXPONENT
C CALCULATE CHANGE IN WAVENUMBERS PER DATA POINT
C IHEAD(17)=SSP
C IHEAD(15)=NTP/256
      DELTA=(15798.2/IHEAD(17))/(128*IHEAD(15))
C DETERMINE SECTORS FOR RANGE 850-1350
      ISEC1=INT(850.0/(DELTA*352))
      ISEC2=INT(1350.0/(DELTA*352))
C
C CALCULATE AND STORE SPECTRUM
C
      DO 500 ISEC=ISEC1,ISEC2
      DO 400 J=1,352
      WAVENUM=(ISEC*352+J-1)*DELTA
C SET DATA TO 0.0 IF OUTSIDE OF RANGE
      IF(WAVENUM.LT.850.0) GOTO 325
      IF (WAVENUM.GT.1350.0) GOTO 325
C CONVERT WAVENUMBERS TO WAVELENGTH IN MICRONS
      W=(1.0E4)/WAVENUM
      WPW=(5.87E-11)*W*SQRT(RN)
      GW=(5.74E-19)*W*RN*RES
      EREAL=11.7-((WPW**2)/(1.0+((GW)**2)))
      ECOM=((WPW**2)*(GW)/(1.0+((GW)**2)))
      RMAG=SQRT((EREAL**2)+(ECOM**2))
      Z=ATAN(ECOM/EREAL)
      IF(Z.LT.0.0) Z=Z+3.14159
      THETA=Z
      ECOEF=SQRT(RMAG)*SIN((THETA/2.0))
      ALPH=4.0*(3.14159)*ECOEF/((1.0E-4)*W)
C CALCULATE TRANSMISSION INCLUDING MULTIPLE REFLECTIONS
      T=(0.49*EXP(-1.0*ALPH*D))/(1.0-.99*EXP(-2.0*ALPH*D))
C CONVERT TO ABSORBANCE
      A=-1.0*ALOG10(T)
      GOTO 350
325   A=0.0
350   XDATA=A*(2.0**(19-IHEAD(6)))
      IDATA(J)=XDATA
400   CONTINUE
```

```
 97.          CALL IWDISK(IDATA,352,FLOC+ISEC)
 98.    500   CONTINUE
 99.          WRITE(2,1000)
100.    1000  FORMAT(' CALCULATION COMPLETE / SPECTRUM STORED IN ORIGIN
100.         $ FILE')
102.          WRITE(2,1100)
103.    1100  FORMAT(' ')
104.          CALL IREXIT
105.          END
```

APPENDIX D

PROGRAM TO CALCULATE THE VACANCY CONCENTRATIONS AS A FUNCTION OF TEMPERATURE AND DOPANT CONCENTRATION

```
1     INTEGER F1,F2
10    INPUT "TEMPERATURE IN DEGREES K",T
30    INPUT "INPUT DONOR DENSITY CM-3",D01
40    INPUT "INPUT Ec-Edonor IN ev",De1
50    INPUT "INPUT ACCEPTOR DENSITY CM-3",A01
60    INPUT "INPUT Eacceptor - Ev IN ev",Ae1
70    Kt=T/11604.5                          ! CALCULATE KT IN EV
101   !CALCULATE ENERGY GAP USING VARSHNI EXPRESSION
102   !SET Ev=0 THEN Ec=Eg
103   Ec=1.17-((4.73E-4*T*T)/(T+636))
104   !
105   !CALCULATE TEMPERATURE DEPENDENT DENSITY OF STATES EFFECTIVE MASS
106   !USE LINEAR APPROXIMATION OF BARBER'S GRAPHS
107 ! Eem=1.2+(T-300)*2.83E-4  !ELECTRON EFFECTIVE MASS
108 ! Hem=.822+(T-300)*3.33E-4 !HOLE EFFECTIVE MASS
109   Eem=1.06
110   Hem=.58
112   !
113   !CALCULATE EFFECTIVE DENSITY OF STATES
114   Nc=(2.509E+19)*(T*Eem/300)^1.5
115   Nv=(2.509E+19)*(T*Hem/300)^1.5
116   !
117   Fp=Ec/2                    !INITIAL GUESS FOR FERMI POTENTIAL
118   De1=Ec/2                   !INITIAL DELTA
120   Ne=Nc*EXP(-1*(Ec-Fp)/Kt)
121   Nh=Nv*EXP(-1*Fp/Kt)
130   D1=D01/(1+2*EXP((Fp-Ec+De1)/Kt))
133   A1=A01/(1+2*EXP((Ae1-Fp)/Kt))
135   V0=5.0E+22*(EXP(-1*2.4/Kt))*EXP(3)
136   V20=(V0*V0/5.0E+22)*4.0*EXP(1.7/Kt)
138   Ev_=.42-(1.17-Ec)
139   Ev__=.876-(1.17-Ec)
140   Ev2_=.51-(1.17-Ec)
141   Ev2__=.77-(1.17-Ec)
143   V_=2*V0*EXP(-1*(Ev_-Fp)/Kt)
144   V__=(V_/2)*EXP(-1*(Ev__-Fp)/Kt)
145   V2_=2*V20*EXP((Fp-Ev2_)/Kt)
146   V2__=(V2_/2.0)*EXP((Fp-Ev2__)/Kt)
148   IF Ne+A1+V_+2*V__+V2_+2*V2__>Nh+D1 THEN GOTO 1000  !CHECK ELEC NEUTRALITY
550   GOTO 1050
1000  F2=1
1010  IF F1=1 THEN De1=De1/2
1020  F1=0
1030  Fp=Fp-De1
1040  GOTO 2000
1050  F1=1
1060  IF F2=1 THEN De1=De1/2
1070  F2=0
1080  Fp=Fp+De1
1090  GOTO 2000
2000  IF De1<1.E-4 THEN GOTO 2020
2010  GOTO 120
2020  Vtotal=V0+V_+V__
2021  V2total=V20+V2_+V2__
2022  Vac_total=Vtotal+2*V2total
2023  PRINT
2025  PRINT
2026  PRINT "TEMP=";T;"DONOR DENSITY=";D01
2027  PRINT
2029  PRINT "FERMI LEVEL=";Fp;" V0=";V0;"V- =";V_;"V-- =";V__;"VTOT=";Vtotal
2030  PRINT
2031  PRINT "V20=";V20;"V2_=";V2_;"V2__=";V2__
2032  PRINT
2033  PRINT "V2TOTAL=";V2total;"****VACANCY TOTAL=";Vac_total
2035  END
```